

NoSOCS in SDSS. II. Mass Calibration of Low Redshift Galaxy Clusters with Optical and X-ray Properties

P. A. A. Lopes^{1*}, R. R. de Carvalho², J. L. Kohl-Moreira³, C. Jones⁴

¹*IPÉD Universidade do Vale do Paraíba, Av. Shishima Hifumi 2911,*

São José dos Campos, SP 12244-000, Brasil

²*Instituto Nacional de Pesquisas Espaciais – Divisão de Astrofísica (CEA), Avenida dos Astronautas, 1758*

São José dos Campos, SP 12227-010, Brasil

³*Observatório Nacional/MCT, COAA, Brasil*

⁴*Harvard-Smithsonian Center for Astrophysics, 60 Garden Street, Cambridge, MA 02138, USA*

Accepted Received ; in original form

ABSTRACT

We use SDSS data to investigate the scaling relations of 127 NoSOCS and 56 CIRS galaxy clusters at low redshift ($z \leq 0.10$). We show that richness and both optical and X-ray luminosities are reliable mass proxies. The scatter in mass at fixed observable is $\sim 40\%$, depending on the aperture, sample and observable considered. For example, for the massive CIRS systems $\sigma_{\ln M_{500}|N_{500}} = 0.33 \pm 0.05$ and $\sigma_{\ln M_{500}|L_x} = 0.48 \pm 0.06$. For the full sample $\sigma_{\ln M_{500}|N_{500}} = 0.43 \pm 0.03$ and $\sigma_{\ln M_{500}|L_x} = 0.56 \pm 0.06$. The scaling relations based only on the richer systems (CIRS) are slightly flatter than those based on the full sample, but the discrepancies are within $1\text{-}\sigma$. We estimate substructure using two and three dimensional optical data, verifying that substructure has no significant effect on the cluster scaling relations (intercepts and slopes), independent of which substructure test we use. For a subset of twenty-one clusters, we estimate masses from the $M\text{-}T_X$ relation using temperature measures from BAX. The scaling relations derived from the optical and X-ray masses are indeed very similar, indicating that our method consistently estimates the cluster mass and yields equivalent results regardless of the wavelength from which we measure mass. For massive systems, we represent the mass-richness relation by a function with the form $\ln(M_{200}) = A + B \times \ln(N_{200}/60)$, with M_{200} being expressed in units of $10^{14} M_\odot$. Using the virial mass, for CIRS clusters, we find $A = (1.39 \pm 0.07)$ and $B = (1.00 \pm 0.11)$. For the same sample, but using the masses obtained by the caustic method, we get $A = (0.64 \pm 0.14)$ and $B = (1.35 \pm 0.34)$. If we consider the mass as estimated from T_X (for the subset of 21 clusters with T_X available) we derive $A = (0.90 \pm 0.10)$ and $B = (0.92 \pm 0.10)$. The relations based on the virial mass have a scatter of $\sigma_{\ln M_{200}|N_{200}} = 0.37 \pm 0.05$, while $\sigma_{\ln M_{200}|N_{200}} = 0.77 \pm 0.22$ for the caustic mass and $\sigma_{\ln M_{200}|N_{200}} = 0.34 \pm 0.08$ for the temperature based mass.

Key words: surveys – galaxies: clusters: general – galaxies: kinematics and dynamics.

1 INTRODUCTION

Two aspects of galaxy clusters make their study uniquely important for cosmology. The path from density perturbations to virialized objects involves the physical mechanisms that ultimately determine the cluster properties as we currently observe them. The growth of these systems depends on cosmological parameters like Ω_m , Ω_λ , σ_8 , etc. The sensitivity to these parameters depends on the redshift (Carroll, Press, & Turner 1992). Therefore, the systematic

study of cluster properties, based on unbiased samples at different redshifts, can provide substantial input for models trying to explain not only how clusters formed and evolved from the astrophysical viewpoint but also how spacetime is structured (e.g. Henry & Arnaud 1991; Rosat et al. 2002). Ultimately, we aim to disentangle the astrophysical aspects from the cosmological ones.

Clusters have no sharp edges. Observations show that their central parts reached virial equilibrium earlier while the outskirts are still accreting matter from their surroundings, making the measurements of cluster properties a difficult issue. Clusters are constituted of both dark (non-

* E-mail: paal@univap.br

baryonic) and luminous (baryonic) matter. This mixture renders observations within a specific wavelength range very limited in utility and determining the physical state of each component too complex. Over the years, the sizes of cluster samples and the quality of the data hampered our progress on all of the fronts mentioned above. Only recently have large samples with high-quality data been obtained, allowing a systematic investigation of these effects (e.g. Vikhlinin et al. 2008; Henry 2004).

The abundance of clusters of galaxies can be used as a probe of linear density fluctuations (Eke et al. 1996) and since their growth is directly determined from the dark energy properties, measuring the number of clusters of a given mass as a function of redshift can constrain the equation of state (w parameter) of this majority component of the Universe (e.g. Frieman, Turner, & Huterer 2001). As shown by Huterer & Turner (2001), the sensitivity of cluster abundance to w is maximum around redshift 1.0, so that a cluster sample over a large area on the sky and deep ($z \sim 1.0$) is critically needed to provide reliable results. Direct measures of halo mass are not possible, so that we have to rely on mass proxies free of systematics. The most accurate mass tracers are velocity dispersion and X-ray temperature. Unfortunately, for large samples, at any redshift, directly measuring these cluster properties is not feasible. Hence, we have to rely on other observables (such as richness or X-ray luminosity) that are easier to derive for all clusters in a given survey.

Several studies have investigated mass-observable (MO) relations and their evolution with redshift in the optical and X-ray (Vikhlinin et al. 2002; Levine et al. 2002; Ettori et al. 2004; Stanek et al. 2006; Becker et al. 2007; Rykoff et al. 2008). As advocated by Lima & Hu (2004, 2005) the variance of the counts themselves (clustering of clusters) can be used to calibrate the MO relation. Dark energy depends only on the redshift, but the cluster properties vary with mass and redshift. Using cosmological simulations one can use counts and their variance to not only normalize the MO relation but also learn which cosmology fits the data better. Therefore, understanding the scaling relations of galaxy clusters and their dependence on the dynamical state of the system is crucial.

This paper focuses on four specific issues: (i) examining the performance of different cluster properties, like richness (N_{gals}), optical (L_{opt}) and X-ray (L_X) luminosities¹, as proxies for cluster mass. The relation between one of these proxies and an independent mass estimate defines a scaling relation; (ii) measuring how much substructure there is in clusters (in 2D and 3D) and establishing its effect on the final mass calibration; (iii) investigating how the scaling relations change when mass is derived from the analysis of the velocity distribution or temperature. Optical masses used in this work are either from a virial analysis (ours) or from the caustic technique (Rines & Diaferio 2006, hereafter RD06); and (iv) comparing the optical and X-ray properties of galaxy

clusters, as well as obtaining a direct relation between R_{200} and richness.

This paper is organized as follows: §2 briefly describes the samples used here, while §3 presents the mass calibration based on N_{gals} , L_{opt} and L_X . In this section we also investigate the effects of substructure on the scaling relations and compare the results based on different mass estimators. These are derived with optical data, from the virial or caustic analysis, or from the gas temperature. The mass-to-light ratio is also presented at the end of this section. In §4 we discuss how our results compare to others in the literature. Correlations between optical and X-ray properties are presented in §5, while in §6 we establish the connection between richness and physical radius. The main conclusions are drawn in §7. The cosmology assumed in this work is $\Omega_m = 0.3$, $\Omega_\lambda = 0.7$, and $H_0 = 100 \text{ h km s}^{-1} \text{ Mpc}^{-1}$, with h set to 0.7.

2 DATA AND METHODS

The main data set used in this work is the supplemental version of the Northern Sky Optical Cluster Survey (NoSOCS, Lopes 2003; Lopes et al. 2004), which has its origin on the digitized version of the Second Palomar Observatory Sky Survey (POSS-II; DPOSS, Djorgovski et al. 2003). In Gal et al. (2004) and Odewahn et al. (2004), we describe photometric calibration and object classification for DPOSS, respectively. The supplemental version of NoSOCS (Lopes et al. 2004) goes deeper ($z \sim 0.5$), but covers a smaller region than the main NoSOCS catalog (Gal et al. 2003, 2009), and contains 9,956 cluster candidates over $\sim 2,700$ square degrees. The smaller area is due to the use of the best DPOSS plates, selected according to seeing and limiting magnitude ($r = 21.0$).

We examine a sample of low redshift galaxy clusters ($z \leq 0.10$) from the NoSOCS supplemental catalog. As this survey comprises mainly poor systems in this redshift range, we complemented them with more massive systems from the Cluster Infall Regions in SDSS (CIRS) sample (RD06). CIRS is a collection of $z \leq 0.10$ X-ray selected clusters overlapping the SDSS DR4 footprint. As described in the first paper of this series (Lopes et al. 2009) we extracted SDSS data for 127 NoSOCS clusters and 56 CIRS systems at low- z .

We used photometric and spectroscopic data from the fifth release (DR5) of the Sloan Digital Sky Survey (York et al. 2000). The exception is for the CIRS systems, which were incorporated in a late stage of this work, thus having data from the SDSS DR6. All the magnitudes retrieved from SDSS are de-reddened model magnitudes. Details regarding SDSS data extraction are provided in paper I (Lopes et al. 2009). There, we used SDSS photometric data to estimate more accurate photometric redshifts (z_{photo} , Lopes 2007), richnesses and optical luminosities for the full NoSOCS supplemental catalog. We found 7,414 systems well sampled in SDSS DR5. Approximately 10% (754) have $z_{\text{photo}} \leq 0.133$ (Lopes et al. 2009).

The above redshift limit comes from the choice of only using clusters at $z \leq 0.10$ for the current work. In this redshift range the SDSS spectroscopic survey is complete. As discussed in Lopes et al. (2009), at higher redshifts galaxy-

¹ The error in the X-ray luminosity presented in the first paper of this series was underestimated. That is fixed in the current paper. All the X-ray measurements available in Table 5 of the first paper are replaced by the values listed in Table A1 of this paper.

ies fainter than $M^* + 1$ are missed, biasing the dynamical analysis (see discussion in section 4.3 of Lopes et al. 2009). Out of the 754 NoSOCS supplemental clusters with $z_{photo} \leq 0.133$, we were able to determine the spectroscopic redshift for 179 systems, requiring at least 3 galaxies within $0.50 \text{ h}^{-1} \text{ Mpc}$ in the SDSS spectroscopic footprint. Note that we only selected systems for which $|z_{photo} - z_{spec}| \leq 0.03(1 + z_{spec})$. We eliminated interlopers using the “shifting gapper” technique (Fadda et al. 1996), applied to all galaxies with spectra available within $2.50 \text{ h}^{-1} \text{ Mpc}$. From the 179 clusters with $z_{spec} \leq 0.10$ we retained 127 systems with at least 10 member galaxies selected by the above procedure. We applied the same procedure to the 56 CIRS clusters. Figures 4 and 5 of Lopes et al. (2009) show the velocity-radius distributions of the 127 NoSOCS clusters and the 56 CIRS systems.

These clusters were then subjected to a virial analysis analogous to the one described in Girardi et al. (1998), Popesso et al. (2005, 2007) and Biviano et al. (2006). This procedure yields estimates of σ_P , R_{500} , R_{200} , M_{500} and M_{200} for the set of 183 low redshift clusters considered in this work. X-ray luminosity is also estimated for these systems using ROSAT All Sky Survey (RASS) data. A detailed description of both the virial analysis and derivation of X-ray luminosity is provided in Lopes et al. (2009), which also lists the properties of these systems in Tables 1, 2, 3, 4, and 5.

The NoSOCS clusters have velocity dispersion estimates of $100 < \sigma_P < 700 \text{ km/s}$. The CIRS systems have $200 < \sigma_P < 900 \text{ km/s}$ (with only 23% of objects with $\sigma_P < 400 \text{ km/s}$). For most of the studies below we ignore three of the CIRS objects which have biased values of σ_P and mass due to projection effects and substructure (see paper I). We only show these objects in Figures 9, 10, and 11, where we investigate the impact of substructure on the scaling relations. These 3 clusters are Abell 1035B, Abell 1291A and Abell 1291B.

3 MASS CALIBRATION

Scaling relations involving a simple cluster observable, like richness or luminosity and a fundamental property such as mass, can provide important clues on how large scale structure forms, galaxy formation proceeds, and how the intra-cluster gas reaches its current state. The establishment of these relations for nearby clusters is also vital for future studies of the cluster population in the distant universe. Particularly, they may help constrain the dark energy equation of state (Majumdar & Mohr 2004).

In this section, we examine the correlation of N_{gals} , L_{opt} and L_X with cluster properties, such as velocity dispersion (σ_P) and mass (M_{200} and M_{500}). We use the spectroscopic redshifts of the clusters (instead of z_{photo}) when computing richnesses and luminosities. Three different apertures are used to derive these quantities: $0.50 \text{ h}^{-1} \text{ Mpc}$, R_{500} and R_{200} . We consider the re-centered (luminosity-weighted) coordinates for the 127 NoSOCS clusters and the original position (X-ray centroid) listed in RD06 for the 56 CIRS clusters. We present the results for the NoSOCS and CIRS samples independently as well as for the combined sample.

In the next three subsections we discuss the mass calibration based independently on richness, optical luminos-

ity, and X-ray luminosity. For the richness relations we also investigate the impact of using less rigorous criteria for interloper removal when computing mass, as well as assuming different centroids and considering all NoSOCS clusters at $z \leq 0.25$. We then examine the impact of cluster substructure on the scaling relations and compare the results derived from mass estimates obtained from different wavelengths. Finally, we show the dependence of the mass-to-luminosity ratio with the cluster scale (defined by its mass).

3.1 Calibration with richness

Figure 1 shows the comparison between mass (M_{500} and M_{200}) with richness, estimated within R_{500} and R_{200} . The lower panels show the residuals, $\text{LOG}(M_{obs}/M_{fit})$. M_{obs} is the observed value of the mass within the given radius, while M_{fit} is the linear regression solution. The results are only shown for the 127 NoSOCS objects. The solid line in each upper panel shows the orthogonal regression fit (Akritas & Bershady 1996). All the scaling relations obtained in this work are of the form

$$\ln(Y) = A + B \times \ln\left(\frac{X}{C}\right), \quad (1)$$

The X and Y parameters are listed in the tables defining the relations (see below). The pivot point (C) depends on the sample being used. It is taken to be approximately the median value of the X parameter within R_{500} for a given sample. For the NoSOCS and full samples (NoSOCS + CIRS) we consider the same pivot point, while for the more massive systems (CIRS) we have another pivot point. Those are listed in the tables and can be seen in the figures. The linear fit is obtained by a two iteration 3-sigma clipping, so that after a first run we eliminate outliers. Those are not used in the final fit and are indicated (if exist) as open symbols in the figures.

The results for the scaling relations involving σ_P , M_{500} , M_{200} and N_{gals} are summarized in Table 1. The columns give (1) the parameters involved in the relation (the abscissa and ordinate of the corresponding plots); (2) the cluster sample used; (3) and (4) the intercept (A) and slope (B); (5) the scatter (in natural log space) in the Y parameter at fixed X; (6) the total number of clusters used in the preliminary fit; and (7) the final number after a 3- σ clip. Note that we evaluated the error in the scatter, performing a bootstrap procedure (500 events) with replacement. So the scatter is shown with the associated error in all tables (exception to Table 8). Rows 1-6 provide the results using only the NoSOCS clusters, as shown in Figure 1. Rows 7-12 are for clusters from RD06 only, while the combination of NoSOCS and RD06 is listed in rows 13-18.

If one has to work within a fixed metric radius, $0.50 \text{ h}^{-1} \text{ Mpc}$ yields the smallest error in the richness or L_{opt} measures and minimizes the scatter in the optical versus X-ray scaling relations (Popesso et al. 2004; Lopes et al. 2006). However, when compared to apertures that scale with mass, this radius ($0.50 \text{ h}^{-1} \text{ Mpc}$) is too large for low mass systems and too small for massive ones, and may lead to tilted (steeper) scaling relations (see Table 1). When we use an aperture that scales with mass the relations become flatter. For instance, for the NoSOCS sample, the slope of the M_{200} - N_{gals} relation is 1.45 when using the fixed metric ra-

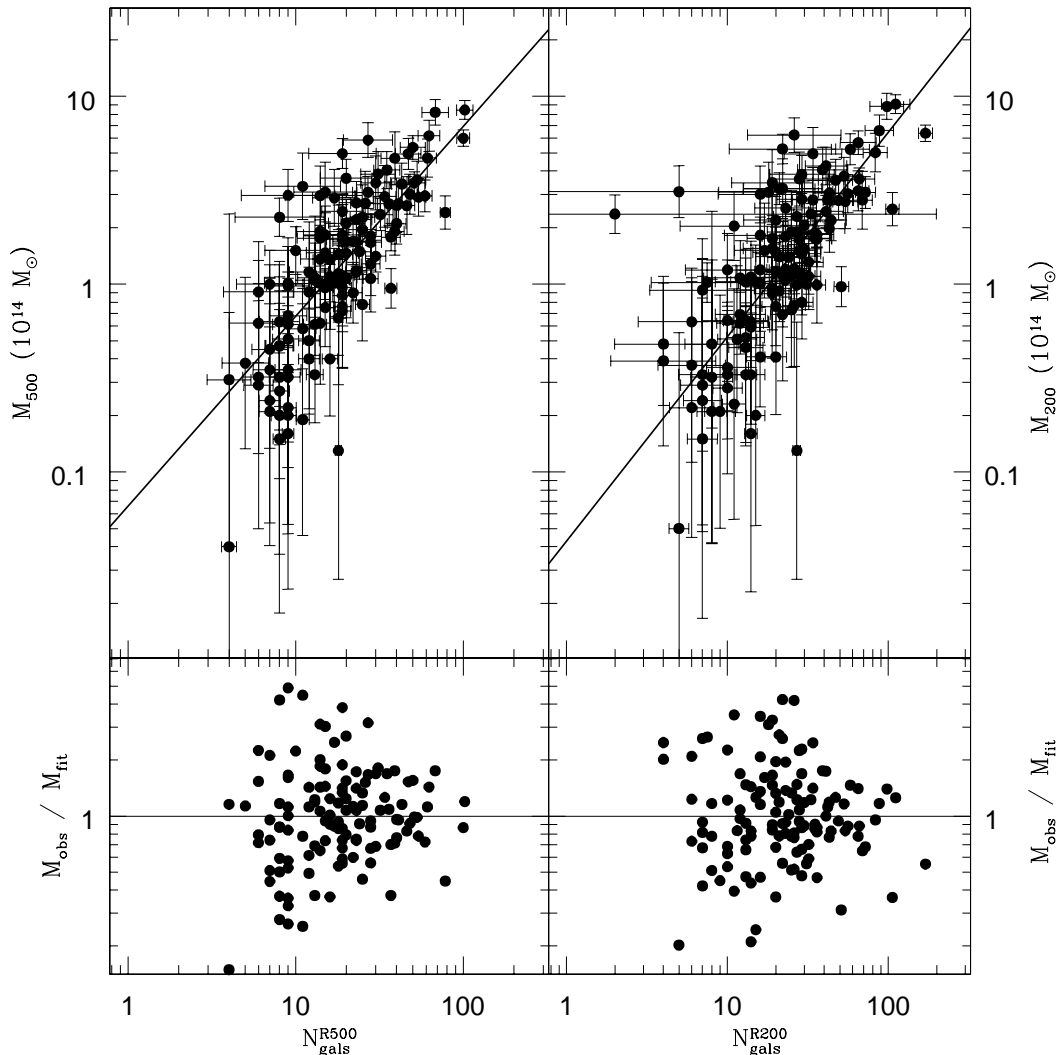


Figure 1. The connection between mass and richness, computed with two apertures (R_{500} and R_{200}). In the lower panels the residuals $\text{LOG}(M_{\text{obs}}/M_{\text{fit}})$ are shown. M_{obs} is the observed value of the mass, while M_{fit} is the linear regression result.

dus for computing richness ($0.50 \text{ h}^{-1} \text{ Mpc}$), but only 1.09 when using R_{200} .

From the lower panels of Figure 1 we see that some of the poorest systems ($N_{\text{gals}}^{R200} < 30$) have larger deviations from the linear solution. Both richness and mass are harder to determine due to the low contrast of some of these clusters. Incompleteness in spectroscopic sampling for these poor systems may also be a problem (see discussion in §3.2).

The comparison of the relations for the 127 NoSOCS clusters, the 53 CIRS systems and the combined sample, shows that the scatter of the relations obtained with the CIRS and extended samples is smaller than for the NoSOCS clusters alone. This is because CIRS is restricted to more massive systems and the enlarged sample has better statistics, spanning a wider range of all parameters. For the M_{200} - N_{gals}^{R200} relation the orthogonal scatter in mass at fixed richness is (0.60 ± 0.07) for NoSOCS, (0.37 ± 0.05) for the CIRS

sample and (0.46 ± 0.04) for the combined data set. The slopes are nearly the same for the NoSOCS and extended samples, but slightly different for CIRS, although they are compatible within the errors. For the M_{200} - N_{gals}^{R200} relation the slope is 1.09 for the NoSOCS sample, 1.00 for CIRS and 1.07 for the combined sample.

3.1.1 Systematics in the scaling relations

Table 2 lists the coefficients of the relations σ_P - N_{gals}^{R200} and M_{200} - N_{gals}^{R200} using only the NoSOCS clusters, with three different methods. In the first two rows we consider the original cluster coordinates instead of the luminosity-weighted ones. Rows 3-4 list the results when we use a more “relaxed” criteria for interloper removal (see § 4.1 of Lopes et al. 2009), and in rows 5-6 we consider all NoSOCS clusters at $z \leq 0.25$, instead of $z \leq 0.10$ (limit adopted for this work). The

latter is useful to see how much the scaling relations are affected for using clusters at redshifts where the spectroscopic sampling is very incomplete (see § 4.3 of paper I). Note that Popesso et al. (2005) (hereafter POP05) considered clusters at $z \leq 0.25$ for deriving scaling relations based on SDSS data.

When comparing the results obtained with the original coordinates (first two rows of Table 2) to the ones with the luminosity-weighted centroids (Table 1), we find that the intercept, slope and scatter are consistent within the errors ($1\text{-}\sigma$). Thus, we conclude that the centroid is not a critical issue when deriving the scaling relations. When the criteria to select interlopers are relaxed (results in rows 3-4 of Table 2) the agreement is not as good for the intercept and slope, but it is still within $1.5\text{-}\sigma$. Relaxing the criteria for rejecting interlopers in the “shifting-gapper” technique has a minor effect in the relations.

The third case in Table 2 uses all NoSOCS clusters at $z \leq 0.25$ (rows 5-6). A comparison to Table 1 reveals that the intercept and slope are now different, in some cases consistent only within $2\text{-}\sigma$. The scatter is, however, similar. This result shows the relevance of using complete spectroscopic samples for studying the scaling relations. The use of clusters at redshifts where the spectroscopic survey is not complete to $M^* + 1$ results in biased velocity dispersion and mass estimates (see paper I), yielding flatter scaling relations.

This is a critical issue for measuring the cluster mass function since the mass calibration might be severely biased. However, it is important to note that this bias in the calibration may reflect the percentage of clusters with incomplete spectroscopic sampling. In this work 127 of the 219 NoSOCS clusters at $z \leq 0.25$ are below $z \leq 0.10$, and are therefore well sampled. Ninety-two of the 219 systems (42%) have poor sampling ($z > 0.10$), a considerable fraction of the total used when deriving the scaling relations. Other authors included $z > 0.10$ clusters in their sample (POP05, for instance), but show results consistent to our unbiased sample (at $z \leq 0.10$). Although they initially have many systems at $z > 0.10$, they require that clusters have at least ten galaxies with redshifts when estimating mass and deriving the scaling relations, which may preferentially exclude many of the higher redshift clusters. We believe that this is the case since their results are consistent with ours.

3.2 Calibration with optical luminosity

Figure 2 shows the comparison between mass (M_{500} and M_{200}) and optical luminosity computed within R_{500} or R_{200} . Residuals are shown in the lower panels. We only show the results for the 127 NoSOCS objects. One interesting feature from the comparison of Figures 1 and 2 (see Tables 1 and 3) is that the slopes obtained in the two cases are consistent. This indicates the optical luminosity and the number of galaxies used to compute L_{opt} , are proportional to each other (see Popesso et al. 2007), with a constant of proportionality consistent with unity. Figure 3 shows σ_P versus L_{opt} , computed within R_{500} or R_{200} for only the CIRS objects. Figure 4 is analogous to Figures 2 and 3, but shows the extended sample of 180 NoSOCS plus CIRS clusters. The inspection of the lower panels of Figures 2 and 4 reveals that larger deviations from the linear regression occur for $L_{opt}^{R200} < 0.30$ $10^{12} L_{\odot}$, corresponding to the cut at $N_{gals}^{R200} = 30$ seen in

Figure 1. Hence, we stress the conclusion that richness, L_{opt} and mass are harder to obtain due to the low contrast of such systems. Another problem affecting these clusters may be incompleteness in the spectroscopic sampling.

To confirm these conclusions we separate the clusters shown in Figure 4 in systems with $|\text{LOG}(M_{obs}/M_{fit})| \leq 2$ or $|\text{LOG}(M_{obs}/M_{fit})| > 2$. We find 135 clusters in the first case and only forty-five (25%) in the second. For $|\text{LOG}(M_{obs}/M_{fit})| \leq 2$ we find the following median values: $N_{gals} = 33.0$, $N_{gals-err}/N_{gals} = 0.24$, $N_{spec} = 48.0$ and $N_{spec200} = 21.0$; where N_{gals} is computed within R_{200} , $N_{gals-err}/N_{gals}$ is the percentage error on the richness measurement, N_{spec} is the number of members (spectroscopically selected) within the maximum aperture (normally 2.5 h^{-1} Mpc; see paper I) and $N_{spec200}$ is the number of members within R_{200} . For $|\text{LOG}(M_{obs}/M_{fit})| > 2$ we have $N_{gals} = 22.0$, $N_{gals-err}/N_{gals} = 0.36$, $N_{spec} = 30.0$ and $N_{spec200} = 15.0$. Thus, the forty-five clusters with larger mass deviations are generally poor, low contrast (indicated by their large percentage error in richness) and have their mass estimates based on few galaxies.

The results shown in Figures 2, 3 and 4 are summarized in Table 3. The meaning of all columns and rows is analogous to those in Table 1. The same conclusions drawn for Table 1 are valid now. The most important result is that the relations involving L_{opt} have approximately the same scatter as those obtained with N_{gals} . In other words, optical luminosity performs as good as richness for mass calibration. For the full sample, the scatter of M_{200} at fixed N_{gals}^{R200} is (0.46 ± 0.04) , while it is (0.49 ± 0.04) at fixed L_{opt}^{R200} . For the CIRS sample, the scatter of M_{200} at fixed N_{gals}^{R200} is (0.37 ± 0.05) , being (0.36 ± 0.06) at fixed L_{opt}^{R200} .

3.3 Calibration with X-ray luminosity

Next we compare the X-ray luminosity estimated in Lopes et al. (2009) to σ_P and mass. As described in paper I, we computed the X-ray luminosity², from RASS, using three different background estimates, termed “annulus” (from a ring surround the cluster), “boxes” (100 randomly selected background boxes) and “frame” (from the whole frame in which the cluster is located). Here we show the results obtained with the “annulus” and “frame” backgrounds.

Figure 5 shows the relation between L_X (“annulus” background) and σ_P (top panels) and mass (lower panels), estimated within R_{500} (left) and R_{200} (right). We lose seventy-four of the 180 clusters from the extended sample, as their X-ray luminosities are upper limits. These are mostly poor systems. When establishing the scaling relations involving L_X , upper limits were not used in the fits. From this plot (and Table 4) we see that the smallest scatter is generally found when using R_{500} .

² Due to a bug in the code used to estimate the X-ray luminosity and its associated error, the background was not properly determined in paper I. That resulted in slightly different values for L_X . However, the errors of L_X were severely underestimated. We fixed the code and updated the values of L_X and its error (for all the three backgrounds) in the current paper. The information given in Table 5 of paper I is now replaced by the data available in Table A1, in the appendix of the present paper.

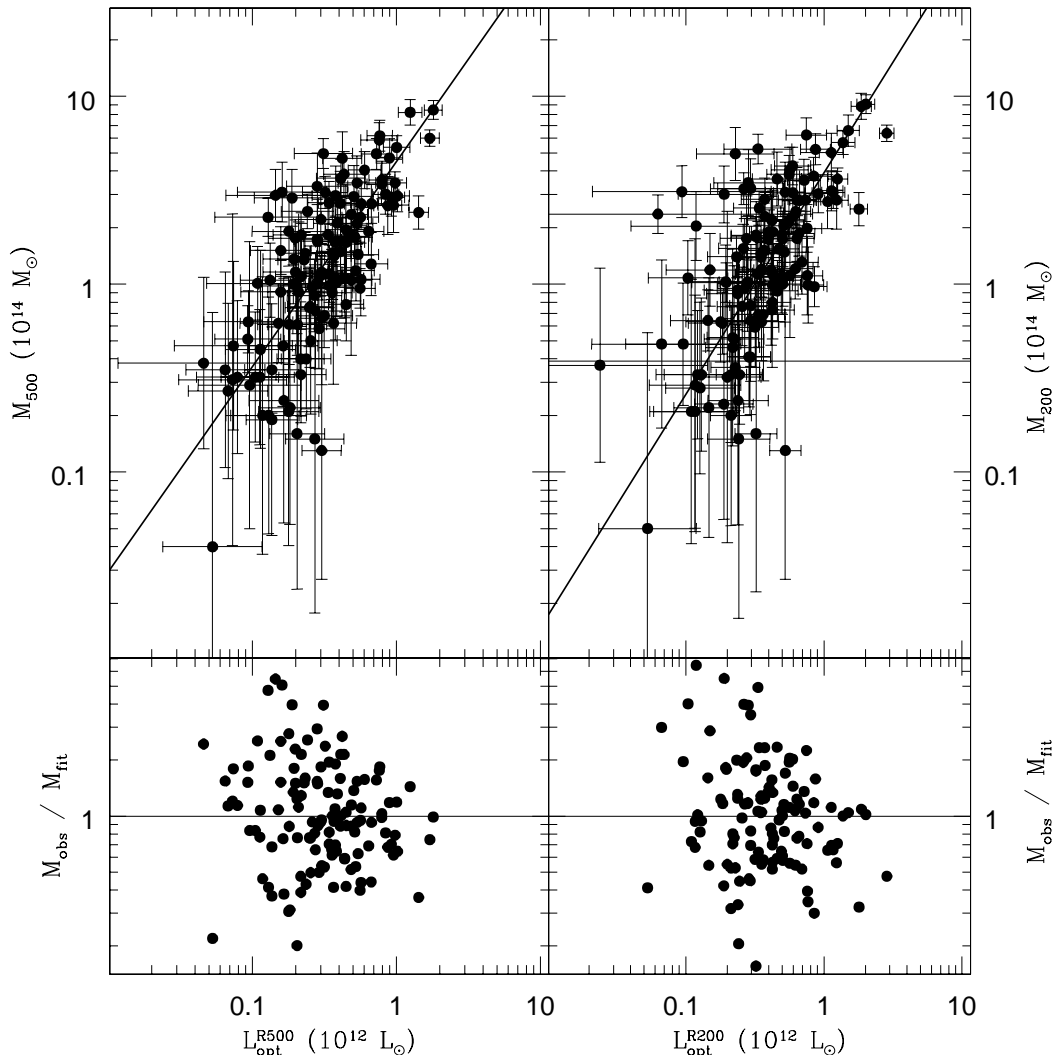


Figure 2. Analogous to Figure 1, but for mass and optical luminosity.

We also studied the relations considering the CIRS subsample, with the comparison of M_{200} and L_X^{R200} shown in Figure 6. It is particularly important to see whether the slope and mainly the scatter are reduced for this sample based on richer clusters. As found for N_{gals} and L_{opt} , the slope also becomes shallower for the richer systems when considering L_X . Note that the slopes are consistent with the full sample (Figure 5 and Table 4) within $1\text{-}\sigma$. The slope of the $M_{200}-L_X^{R200}$ relation is (0.67 ± 0.06) for all clusters and (0.52 ± 0.08) for CIRS (see Table 4). The scatters in the relations based on the richer clusters are slightly smaller than those of the whole sample, but still within $1\text{-}\sigma$. The relations based on the “frame” background are similar to the ones obtained with the “annulus”, being the agreement within $1\text{-}\sigma$. Figures 7 and 8 show the results with the “frame” background, for the full and CIRS samples, respectively.

Tables 4 and 5 summarize the relations involving L_X . Table 4 gives the results for the “annulus” background, while

Table 5 is for the “frame” background. As in the previous tables, the first column lists the two parameters being compared. The background type is listed in the second column. The sample used is in the third column, while the remaining columns are analogous to Table 1. In both tables we list the results for the full sample and for the CIRS systems.

When comparing the performance of optical parameters (richness or L_{opt}) to L_X as a trace of the cluster mass, we find that the former perform a little better than the latter. However, in the worst cases, the scatter is consistent within $1.5\text{-}\sigma$ (see Tables 1, 3, 4 and 5). The main reason for these minor differences may lie in the fact that RASS data is shallower than the optical data from SDSS, so that L_X is determined less accurately than N_{gals} and L_{opt} . It is also important to stress that the optical properties may be used as reliable mass proxies, in the same way as L_X . This finding corroborates the results from POP05, who found that

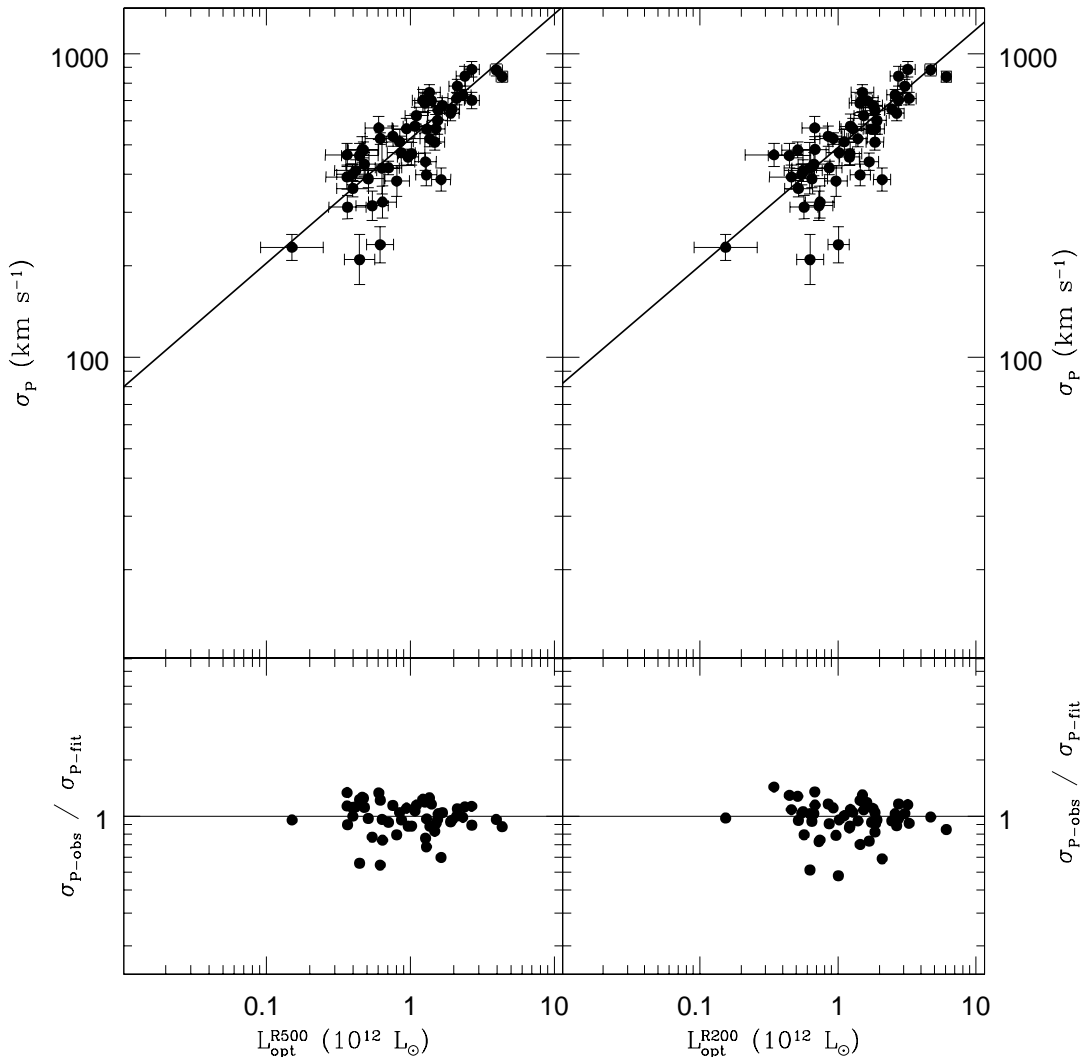


Figure 3. Analogous to Figure 2, but using only the 53 clusters from RD06 and considering σ_P and L_{opt} .

L_{opt} gives slightly more accurate results than L_X (also using SDSS and RASS data).

3.4 Impact of substructure in the scaling relations

In Lopes et al. (2009) we described the use of photometric and spectroscopic data for NoSOCS and CIRS clusters to estimate the fraction of systems with substructure. Two specific tests have proven to be very sensitive to the presence of such disturbances in the galaxy distribution inside a cluster (Pinkney et al. 1996). The first test is the DS, or Δ test (Dressler & Shectman 1988), which is a three dimensional test. The second is a two dimensional test, called the symmetry or β test, introduced by West et al. (1988). Detailed descriptions of both tests can be found in Pinkney et al. (1996) and Lopes et al. (2009). For both tests, the significance level is determined with the aid of Monte Carlo simulations. We set our significance threshold at 5%.

The substructure tests are only applied to clusters with at least five galaxies within the aperture being considered. In paper I we showed that when using an aperture of R_{200} the rate of clusters showing significant signs of substructure is $\sim 21\%$ for both the Δ and β tests. The latter can be applied to galaxies with spectra or to the photometric data alone, while the former test requires redshifts. If we apply the β test to the galaxies within a fixed metric aperture ($1.5 h^{-1}$ Mpc) the rate of clusters with substructure rises to $\sim 35\%$, in line with Lopes et al. (2006), who estimated substructure from two dimensional optical data for $> 10,000$ clusters.

In this work we do not intend to investigate substructure for each cluster individually. Our goal is to check the possible effect of substructure on the scaling relations connecting M_{200} to N_{gals} and L_{opt} . Four different cases are considered. First we apply the Δ test to the 170 clusters with at least five galaxies with z_{spec} within R_{200} . Second, we apply the β test to the same data set. Third, the β test is applied

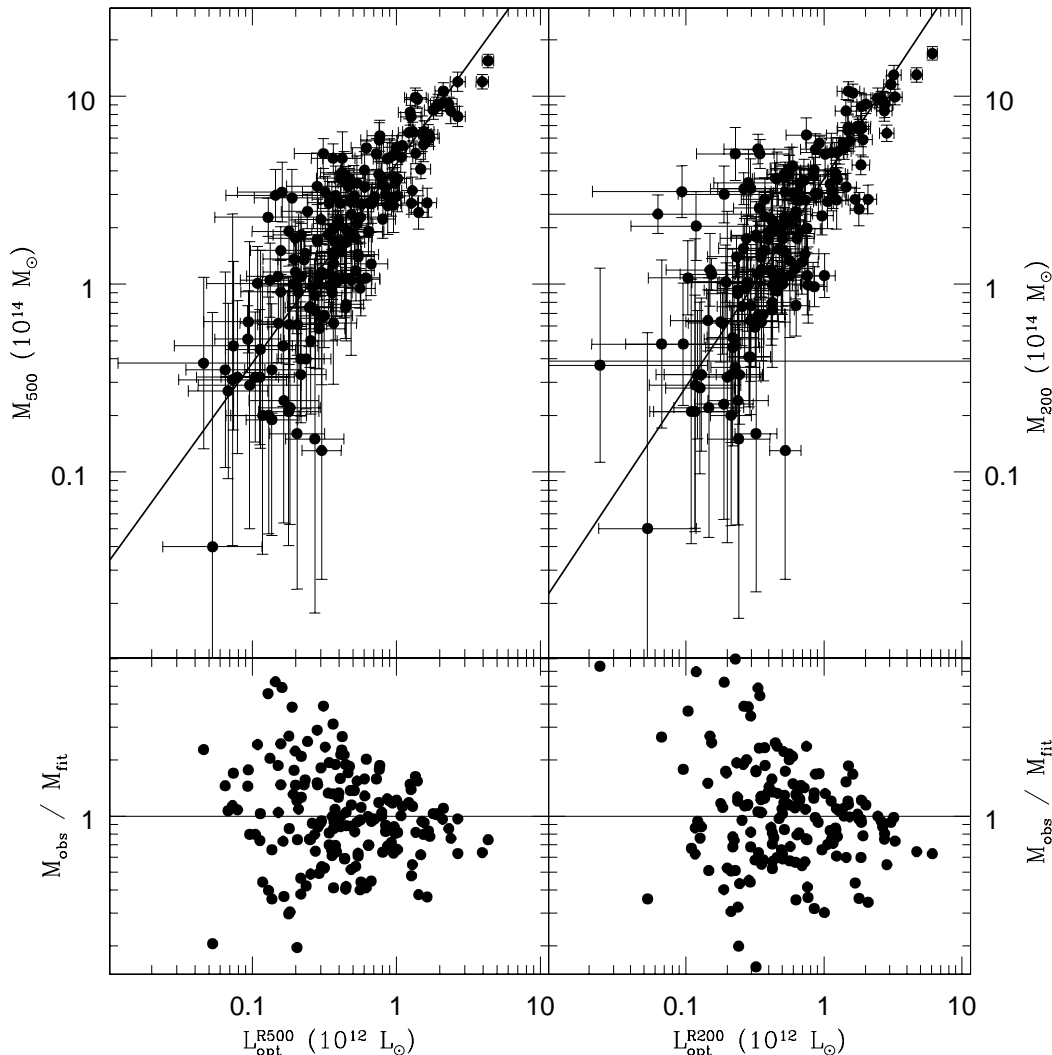


Figure 4. Analogous to Figure 2, but for the combined sample of 127 NoSOCS clusters and 53 systems from RD06.

to the photometric galaxy distribution within R_{200} . We consider all galaxies with $m^* - 1 \leq m_r \leq m^* + 1$ (see Lopes et al. 2006 for details) with no restriction regarding z_{spec} . Fourth, we apply the β test to all galaxies within $1.5 h^{-1}$ Mpc of each cluster (the same photometric range is enforced).

The results for the cases listed above are summarized in Table 6. In this table we always show first the results for the full sample and then the ones for clusters without substructure. The first six lines give the results considering the first two cases mentioned above. Lines 7 to 10 list the results for the third case, and the last four lines summarize the results for the fourth case. The first column lists the two parameters of the scaling relation (and the aperture adopted for computing N_{gals} and L_{opt}). The second column shows the substructure test (if any) used to remove clusters with substructure. Note that the aperture used for estimating substructure is R_{200} in the first three cases and is $1.5 h^{-1}$ Mpc for the fourth. The sample used is listed in column 3.

The meaning of the remaining columns is the same as in Table 3.

Figures 9, 10, and 11 show the results for the first, third and fourth cases discussed above. In each figure the relation between σ_P (top) and M_{200} (bottom) to L_{opt} is displayed for all clusters (left) and for the substructure-free systems (right). From Table 6 and Figures 9 and 10 we see that the fitting parameters and scatter of the scaling relations, depend very little on the presence of substructure. The intercepts and slopes are always consistent within $1\text{-}\sigma$. It is important to note that the 2D and 3D tests indicate similar fractions of clusters with substructure, and the scaling relations obtained for the substructure-free systems are nearly the same as those for the full sample, regardless of whether the test used to detect substructure is 2D or 3D.

From Figure 11 we see that even considering the full photometric data within a fixed radius, instead of only cluster members within R_{200} , the results are qualitatively the

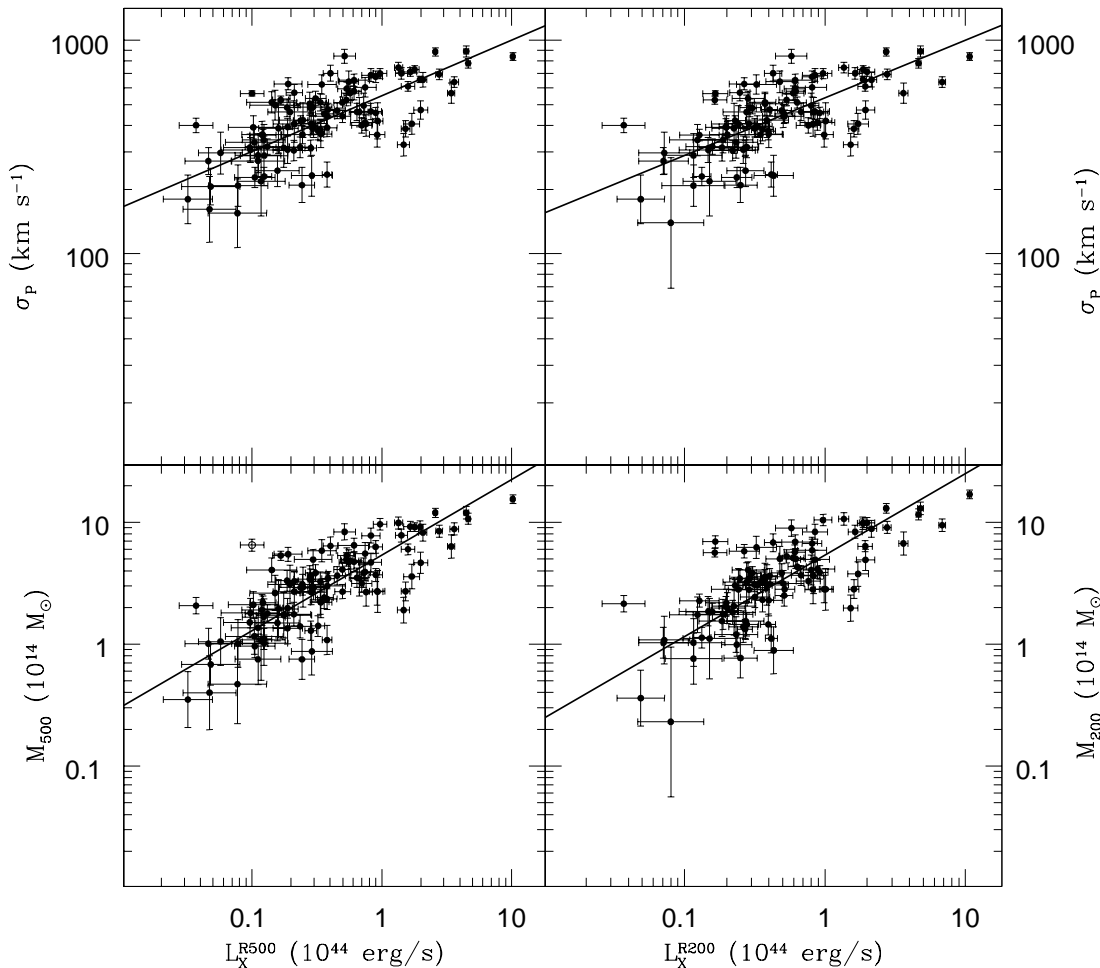


Figure 5. The correlation between σ_P , mass, and X-ray luminosity (estimated with the “annulus” background). The 76 clusters with upper limits (UL) for L_X are not included in the plot or used for the fitting.

same. Due to the different apertures the scaling relations are different from the two previous figures. However, we still find the relations to be insensitive to the exclusion of clusters with substructure. The scatter of the relations (with or without substructure) shows a larger difference than for the other cases above, but it is still within $1\text{-}\sigma$. These results contradict Figure 16 of Lopes et al. (2006), where a strong segregation in the $T_X\text{-}N_{gal}$ relation was caused by the presence of substructure in some clusters. Several reasons may be responsible: 1) T_X was taken from the literature, so the estimates may be very heterogeneous; 2) T_X was not available for the poorer clusters ($N_{gal} < 20$); and 3) the small sample size used in that work makes the results sensitive to the exclusion of a few points.

We repeated the analysis presented in Figure 11 but only for clusters with $N_{gal} \geq 20$ and found that the scatter of the relations decreased only by 5%. However, the slope

exhibited a significant variation ($\approx 27\%$). So, the strong segregation present in the $T_X\text{-}N_{gal}$ relation of Lopes et al. (2006) may be explained by the small sample size and the exclusion of poor systems ($N_{gal} < 20$). In Lopes et al. (2009), we checked that the T_X values derived from BAX represent a consistent data set, which implies that the main source of slope variation detected is the absence of low mass systems.

3.5 Comparison of scaling relations derived with optical and X-ray mass estimates

As described in Lopes et al. (2009) we have searched BAX (*Base de Données Amas de Galaxies X*, <http://bax.ast.obs-mip.fr/>) for counterparts to the 183 clusters used in this work. The search was restricted to objects at $z < 0.12$ with X-ray temperature measures. We found 282 clusters in BAX, of which 21 are common to

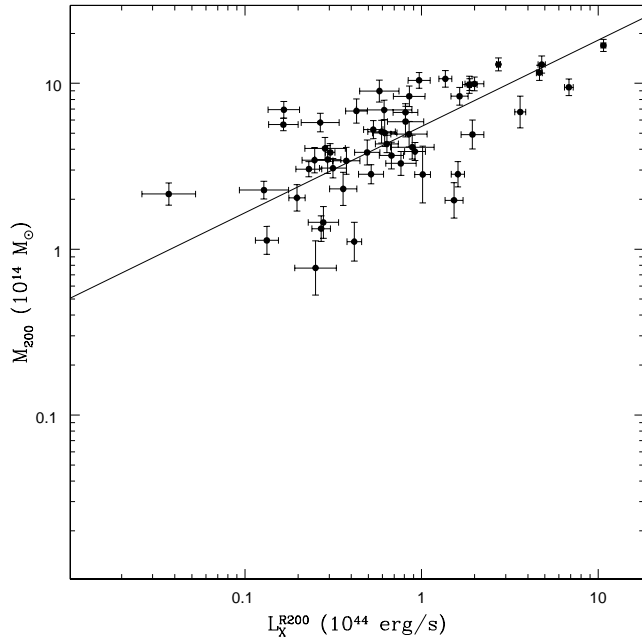


Figure 6. Analogous to the previous figure, but showing only the relation M_{200} - L_X^{R200} for the 53 CIRS clusters.

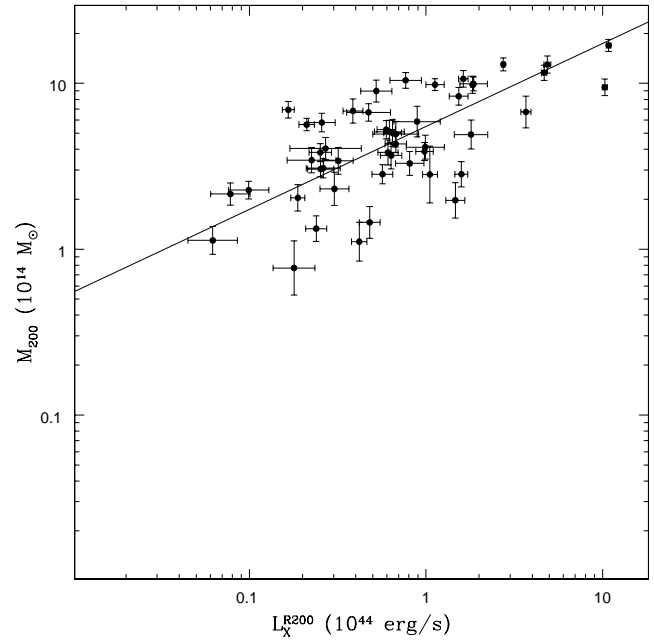


Figure 8. Analogous to the previous figure (“frame” background), but showing only the CIRS clusters.

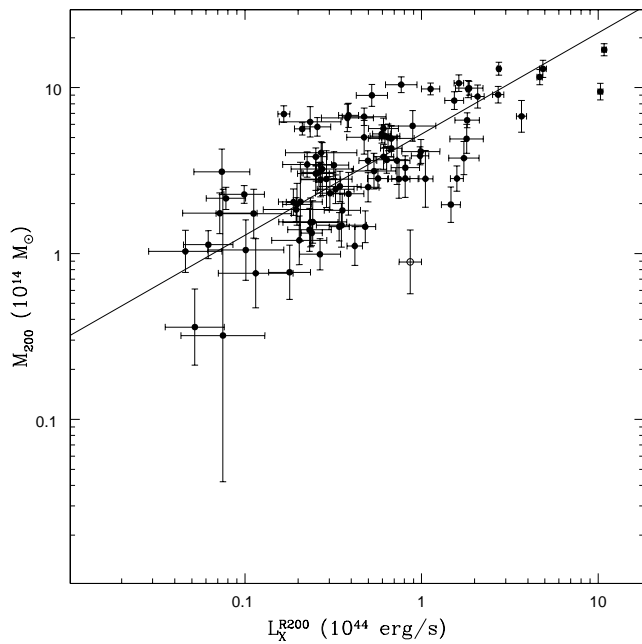


Figure 7. Analogous to Figure 5, but showing only the relation M_{200} - L_X^{R200} for the full sample and with the “frame” background.

our sample. For these clusters, we employed the M_{200} - T_X relation given by equation 3 of POP05 to estimate masses. Our goal is to check if the mass calibration gives the same results when using either the optical or X-ray masses. Of the 183 NoSOCS plus CIRS systems, temperatures are

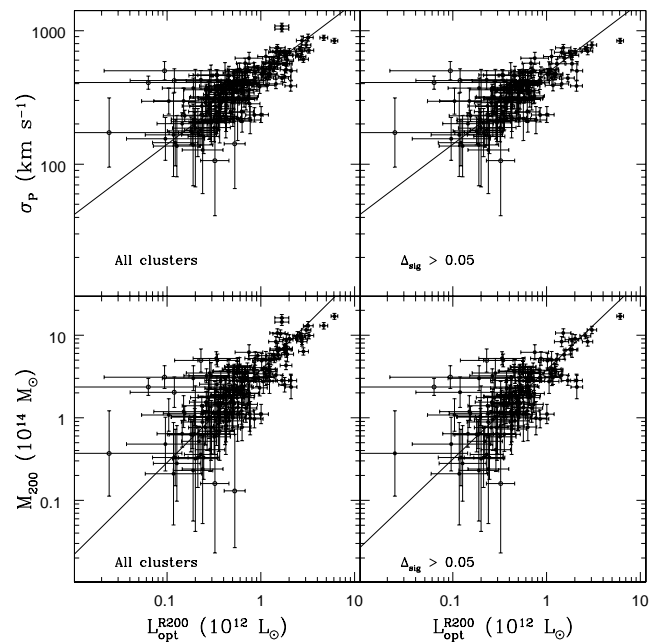


Figure 9. The relations σ_P - L_{opt}^{R200} (top panels) and M_{200} - L_{opt}^{R200} (bottom panels) are shown for all clusters (left) and systems without significant evidence for substructure (right). We apply the Dressler-Schectman (or Δ) substructure test to the spectroscopic sample of 170 clusters with at least 5 galaxies (with spectra) within R_{200} . Of these, 39 ($\sim 23\%$) clusters shown strong signs of substructure.

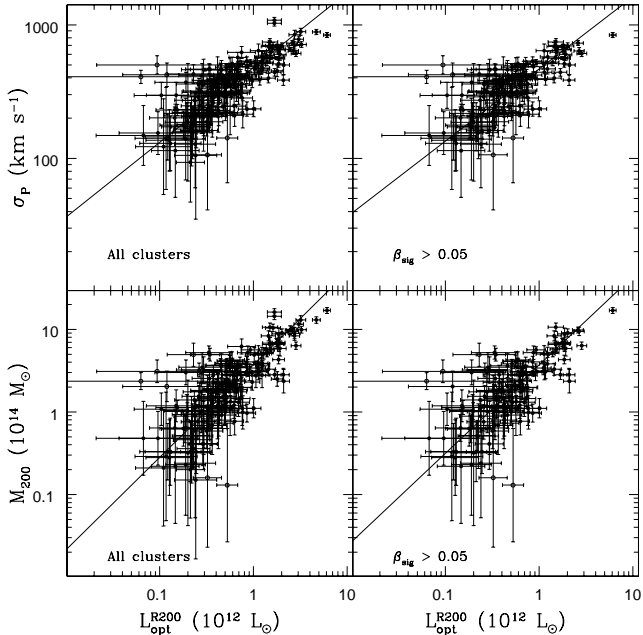


Figure 10. Analogous to the previous figure, except for the data set and substructure test employed. Now we use the symmetry (or β) substructure test applied to the photometric data ($m^* - 1 \leq m_r \leq m^* + 1$) for the 179 clusters with at least 5 galaxies within R_{200} . This is a two-dimensional (2D) test. Out of the 179 clusters, 43 ($\sim 24\%$) systems are found to have substructure.

generally available only for the more massive clusters, with $\sigma_P > 400$ km/s or $M_{200} > 10^{14} M_\odot$.

In Lopes et al. (2009) we show that the temperature values selected from BAX represent a consistent data set. There, we compare the values listed in BAX to the ones available in RD06, finding that most systems agree within 10%. We also check that the masses obtained from the dynamical analysis of the optical data generally agree within 40% of the estimates derived from the M_{200} - T_X relation. The exceptions, most of times, are clusters affected by substructure. When using the optical masses derived with the caustic technique (RD06) the agreement is not as good, with the optical masses being lower than the X-ray values in the low-mass regime.

In this section, we check if the scaling relations obtained in this work are similar to the ones using mass derived from the tight connection to T_X . As the velocity dispersions and masses obtained with the caustic technique are provided by RD06 we also compare our results to those based on their estimates. Figures 12 and 13 show the M_{200} - L_{opt} and M_{200} - L_X relations, respectively. L_X is the value derived in this work with the “frame” background, using RASS data. Both figures consider M_{200} as determined from T_X (equation 3 of POP05). These results are summarized in the first four lines of Table 7, where we also list the fit parameters for the M_{200} - N_{gal} relation and for M_{200} - L_X (considering the “annulus” background).

From inspection of this table, and considering the range of clusters sampled, the results are in very good agreement to those based on the virial mass and restricted to the richer clusters. In Tables 1, 3, 4 and 5 the CIRS sample repre-

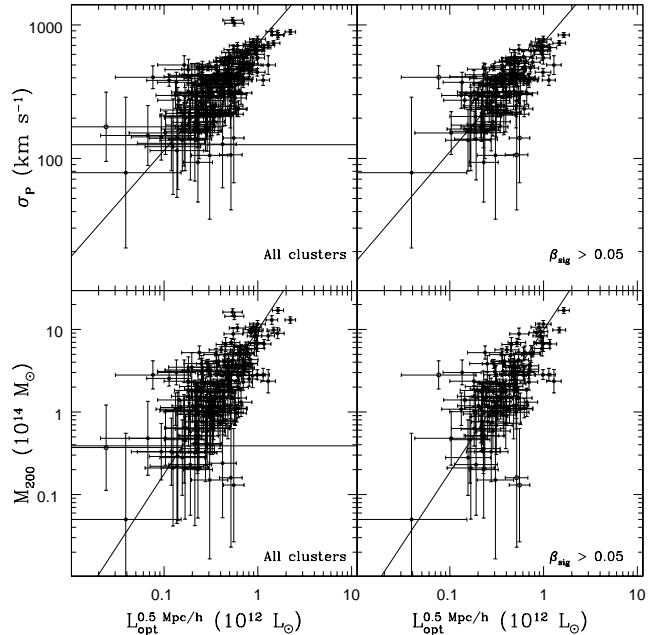


Figure 11. Analogous to the previous figure, except for the sample of galaxies considered. The β test is used again. However, we consider the values of L_{opt} computed within $0.5 h^{-1}$ Mpc and the substructure results obtained within $1.5 h^{-1}$ Mpc. The choice of optimal sizes of the fixed aperture for counting galaxies and the way we estimate substructure are both explained in Lopes et al. (2006). The β test is applied to all 183 clusters of the NoSOCS and CIRS sample. We find that 64 ($\sim 35\%$) clusters show signs of substructure.

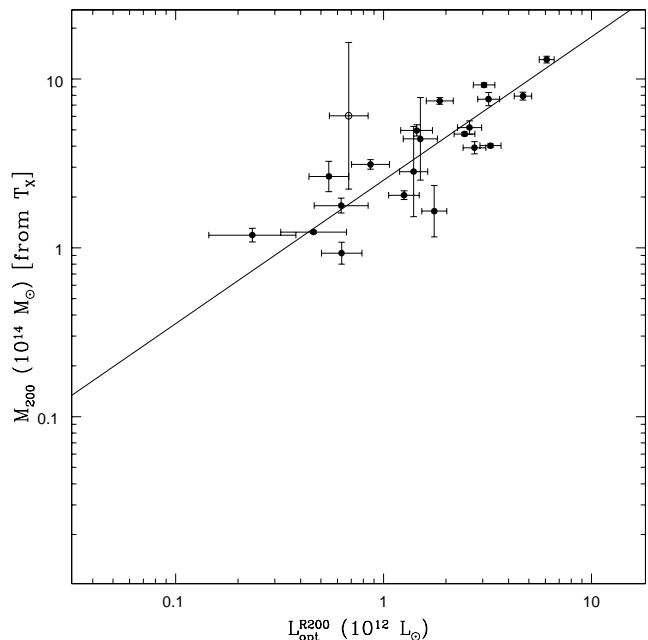


Figure 12. The relation between mass estimated from X-ray data and optical luminosity.

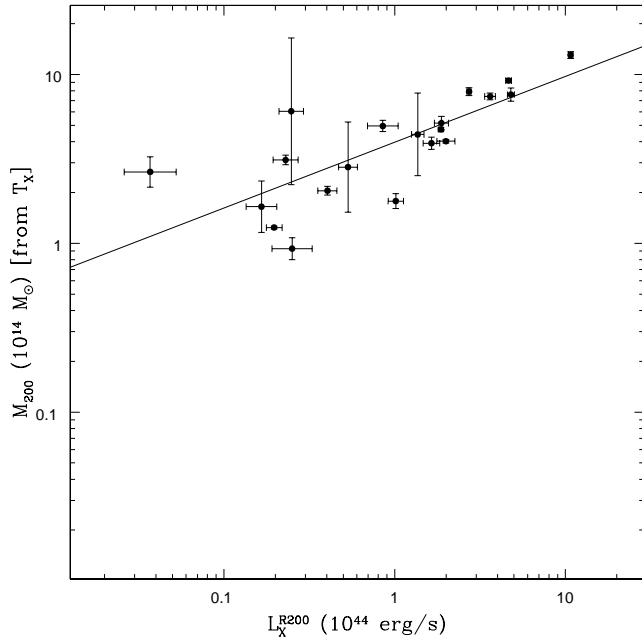


Figure 13. The relation between mass estimated from T_X and X-ray luminosity. L_X is the one determined in this work, considering the “frame” background.

sents the richer clusters. Although the sample with masses derived from T_X (Table 7) is less than half of our rich sample, we conclude that using the optical or X-ray mass leads essentially to the same scaling relations. In particular, the slopes are always concordant within $1-\sigma$. It is imperative to compare the results in Table 7 to those of the rich samples of the previous tables, which have approximately the same mass range.

Note also that the scatters of the relations in Table 7 are generally smaller than what we found with the virial masses. However, the results agree within $1-\sigma$. The improvement is more pronounced only for the relations involving L_X , reaching half the scatter for the “frame” background (but still within $2-\sigma$). These more accurate results are due to the smaller sample size of the relations based on the mass obtained from T_X (only 21 clusters). The most important conclusion from this exercise is that N_{gals} , L_{opt} and L_X can be used for mass calibration and the results are independent to the way mass is estimated, from optical (virial analysis) or X-rays (using the M- T_X relation).

We decided to investigate if these conclusions hold for the parameters derived from the caustic technique (RD06). Figures 14, 15, 16, and 17 show the M_{200} - N_{gals} , M_{200} - L_{opt} , M_{200} - L_X and σ_P - L_{opt} relations, considering mass and σ_P obtained with the caustic technique. These parameters are provided for all CIRS clusters in RD06. Richness, optical and X-ray luminosities are estimated in the present work. These relations, as well as σ_P - N_{gals} and σ_P - L_X , are summarized in the last eight rows of Table 7.

When comparing these relations to the results in Tables 1, 3, 4 and 5 (only for the CIRS systems) the normalizations show better agreement than above. This is due to the fact that all the comparisons use only the CIRS sample. The

slopes agree within $2-\sigma$ for the relations involving σ_P and within $1-\sigma$ for those regarding M_{200} . However, this only happens because the uncertainties in the fit parameters of the relations involving mass are much larger than the ones regarding σ_P . The uncertainty in the slopes of the relations using the caustic mass is also larger than what we found with the virial mass, by as much as a factor of three. So, although the relations based on our masses (or the X-ray derived masses) agree within the errors to those obtained with the caustic method, the nominal values are very different. When using the caustic parameters, the relations about σ_P have smaller slopes compared to ours. The opposite is true for the relations regarding M_{200} .

We also find that the relations based on the caustic values are noisier (with larger scatter) than ours, especially for results involving mass. This is easily seen in Figures 14-17 and Table 7. For instance, for the M_{200} - L_{opt}^{R200} relation the scatter in mass at fixed luminosity is (0.74 ± 0.18) when using the CIRS values, but only (0.36 ± 0.06) for the virial masses determined in the current work.

Such findings are explained by the fact that our velocity dispersions are in good agreement with those of RD06, as shown in paper I. However, the same is not true when comparing masses. Those masses estimated from T_X also disagree with the caustic values. RD06 claim concordance between the caustic results and their virial masses (as well as the X-ray estimates). However, comparing our masses and the caustic values (RD06) to the X-ray estimates, we find a better correlation with our values. Therefore, we conclude that our estimates better represent the cluster potentials, as discussed in Section 6 of paper I. There, we also argue that the interloper removal procedure should not be responsible for the different results (as the velocity dispersions are similar between our work and RD06).

The culprit for the different mass estimates lies in the discrepant values of R_{200} , which in RD06 are derived from the caustic mass profile. In paper I we estimate R_{200} as a by-product of the virial analysis and the assumption of an NFW profile (Navarro et al. 1997). This profile is well matched to the caustic mass profile for only half of the CIRS sample (RD06), which may explain the different results and the larger scatter for the caustic based scaling relations. Note also that RD06 use R_{200} determined by the caustic to compute the virial masses. That choice helps improving the agreement they find between the caustic and virial masses. The conclusions we reached in paper I (Lopes et al. 2009) are corroborated by the scaling relations shown above.

3.6 The mass-to-light ratio

In this section, we present the mass-to-light ratio (M/L) of clusters of galaxies. That has been used before for estimating the mass density of the universe. The typical value of M/L for rich clusters is $M/L \simeq 300 h M_\odot/L_\odot$ (Bahcall & Comerford 2002). Previous works have shown that M/L increases with the size of the bound systems, from galaxies to clusters. The dependence of the cluster M/L ratio on cluster mass can be parametrized by a relation like $M/L \propto M^\alpha$, with $\alpha \simeq 0.20$ (Bahcall & Comerford 2002; Popesso et al. 2005).

In Figure 18, we show the mass-to-light ratio obtained in this work. We recomputed L_{opt} considering the interval

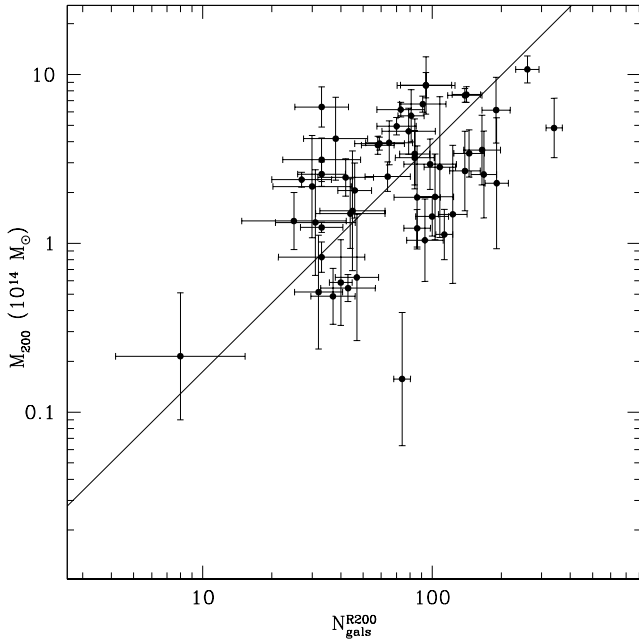


Figure 14. The connection between the caustic mass (RD06, estimated from the optical data) and richness. The relation is exhibited for the 53 CIRS clusters.

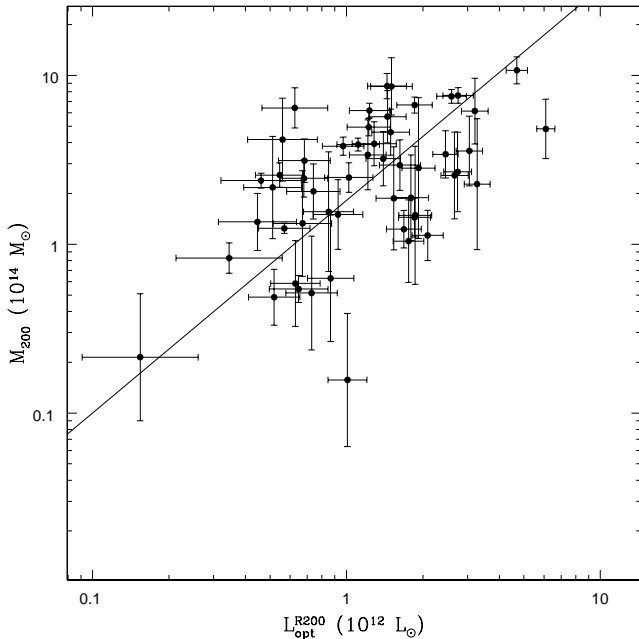


Figure 15. Analogous to previous figure, but showing L_{opt} .

of m^*-5 to m^*+5 . Using the values obtained in paper I and considering the same range used for the richness estimation (m^*-1 to m^*+2), would lead to M/L values that are too high. We do not consider an incompleteness correction to the luminosity function (LF) for galaxies fainter than m^*+5 as the correction is around 5% and uncertainties in the slope

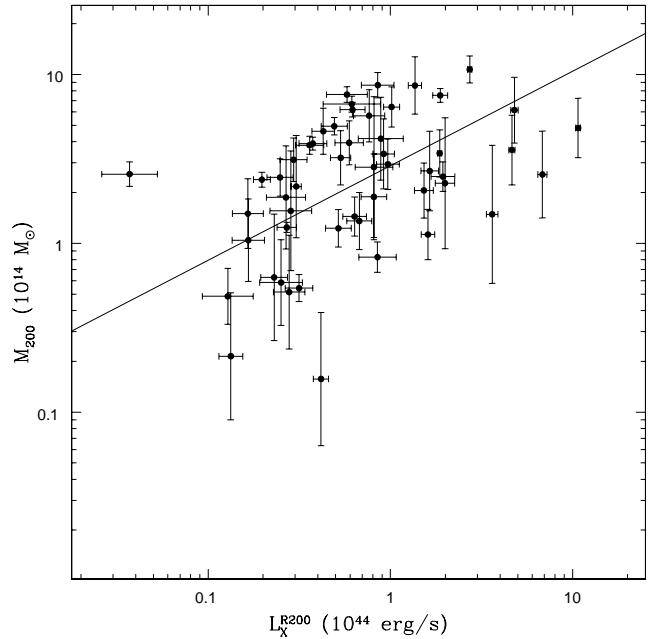


Figure 16. The relation between the caustic mass (RD06) and X-ray luminosity. L_X is obtained with the “annulus” background.

at the faint end of the LF could bias the L_{opt} values. So, integrating the LF to infinity does not significantly change L_{opt} . The range we considered is already deep enough (being five magnitudes fainter than m^*). In Figure 18, the solid line shows the relation listed in Table 3 for ALL clusters, while the other two are based in Popesso et al. (2005). The dotted line considers their “optical” sample (69 clusters with optical masses), while the dashed line is for their “enlarged” sample, with 102 clusters comprising the optical sample plus clusters with masses estimated from the M- T_X relation. All the lines are normalized to an M/L ratio of 200.

As we can see from Figure 18 our results show good consistency to previous findings, reinforcing the dependence of the M/L ratio to the cluster scale. Note that the power of the relation we find is $\alpha = 0.10$, smaller than the value of 0.19 from Popesso et al. (2005) (“optical” sample; dotted line). However, both results are consistent within $1-\sigma$ and we find nearly the same slope as represented by their “enlarged” sample ($\alpha = 0.09$; dashed line). The mean M/L ratio we find is ~ 210 , in excellent agreement to previous studies (Bahcall & Comerford 2002). In a future work we plan to investigate the LF function of clusters in detail and in conjunction to the mass-to-light ratio and its dependence on cluster mass.

4 COMPARISON TO THE LITERATURE AND DISCUSSION

The results in Tables 1, 3, 4 and 5 indicate a good agreement with most findings in the literature. In Table 8 we summarize our main results, considering all clusters, or only the CIRS systems, as well as the findings of other authors. In particular, there is good consistency between the slopes

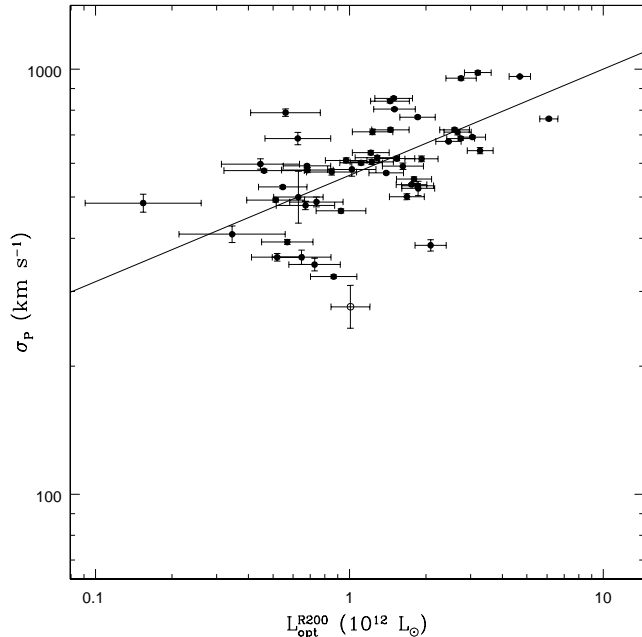


Figure 17. The relation between velocity dispersion estimated with the caustic technique and optical luminosity. The relation is shown for the 53 CIRS clusters.

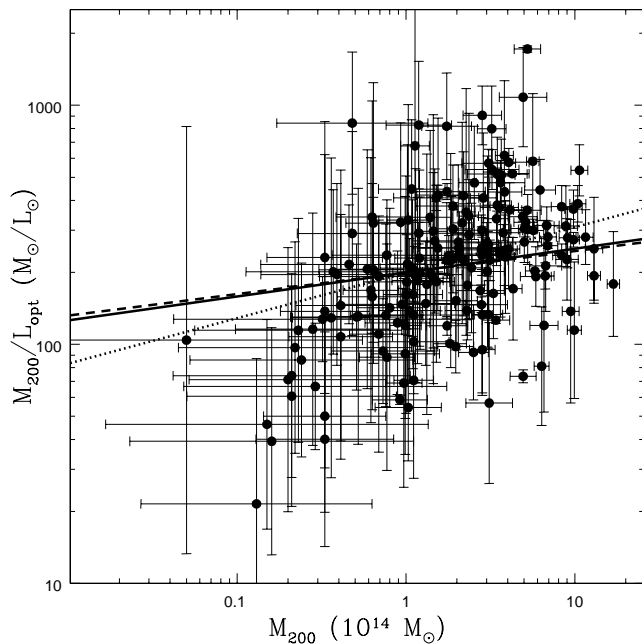


Figure 18. The mass-to-light ratio for the 127 NoSOCS plus 53 CIRS clusters. The solid line shows the relation listed in Table 3 for ALL clusters. The other two results shown are from Popesso et al. (2005). The dotted line considers their “optical” sample, while the dashed line is for their “enlarged” sample. All the lines are normalized to a M/L ratio of 200.

and scatter of POP05 (also based on SDSS and RASS) with our results, in the worst cases within $1.5\text{-}\sigma$. RD06 claim to find good consistency with POP05. However, as seen in the previous section that is at the cost of larger errors for the fit parameters and much noisier relations. Note that our results based solely on CIRS (the most massive systems) always have smaller slopes (an issue we discuss further below). Using an enlarged data set Popesso et al. (2007) found relations consistent to POP05.

The works of POP05 and RD06 are the easiest comparison to ours, since they are also based in SDSS data. However, other results, based on different surveys and wavelengths can be informative. Lin, Mohr & Stanford (2004) found $M_{200} \propto L_{K,R200}^{1.22}$ and $M_{200} \propto N_{gal,R200}^{1.15}$, using Two Micron All Sky Survey (2MASS) data. Our slopes agree within 1.5 and $1\text{-}\sigma$, respectively. Note that we consider their results after excluding the BCG, as they claim better agreement on the powers of the two relations. Kochanek et al. (2003) found $M_{200} \propto N_{*,666}^{0.91}$, also using the 2MASS K-band, a result that agrees with ours within $1.5\text{-}\sigma$. These findings corroborate the conclusion of Popesso et al. (2007), who reports no significant difference among results in different SDSS bands. So, even considering the 2MASS K-band it seems that the results are similar.

On what regards other works using L_X as a mass tracer, we find that the slopes of Popesso et al. (2005); Stanek et al. (2006); Vikhlinin et al. (2008) and Ettori et al. (2004) are consistent to ours. The scatter is consistent (within $1\text{-}\sigma$) to the works of Popesso et al. (2005) and Stanek et al. (2006), while the scatter from Vikhlinin et al. (2008) and Ettori et al. (2004) are smaller than ours (consistent only within $3\text{-}\sigma$). Note that the first two works above (Popesso et al. 2005; Stanek et al. 2006) are based in the RASS data, while the last two use the Chandra satellite. We find a very good agreement (within $1\text{-}\sigma$) between the normalization we measure and the results of Popesso et al. (2005), for the M- L_X relation. Differences in the normalization to the other works above might be due to the differences in the cluster samples used, which may span different mass/luminosity regimes. The comparison of the different selection functions is very hard and is not our goal in this work.

The small differences with POP05 still deserve a few comments. The scatter in M_{500} at fixed L_{opt}^{R500} is similar to ours (consistency within $1.5\text{-}\sigma$). However, a closer look at the upper left panel of our Figure 4 and their Figure 5 shows that we have many more clusters at $M_{500} < 10^{14} M_\odot$ than they do. So, their results are based on a data set showing a cloud of points at $M_{500} > 10^{14} M_\odot$ and a few scattered systems below this value. Nonetheless, that small data set in the low mass regime is sufficient to put their results and ours at the same level. One odd aspect of their plot is the diffuse distribution of the high mass systems, showing high scatter in this mass regime. Our relations always show a reduced scatter towards higher mass. Their poor sampling at low masses can also be seen in Figures 11 and 13 of their work, where we note a deficit of clusters below $\sigma_P = 400$ km/s.

Considering this sampling issue in POP05 it is natural to compare their results with the ones we obtained using only CIRS (which also has mostly clusters with $\sigma_P > 400$ km/s). Figure 3 shows the relation between σ_P and L_{opt}^{R200} .

It is remarkable how low the scatter is in this figure. However, the most interesting point is that the relations are slightly flattened for the CIRS clusters, when compared only to NoSOCS or all systems. So, it seems that the scaling relations have different behaviors in different mass regimes. They look steeper for the low-mass systems, becoming flatter for the high-mass clusters. Using CIRS we note that the agreement to POP05 is as good as before, despite the fact the slope is now smaller.

Popesso et al. (2007) created a larger sample by adding 130 Abell clusters with confirmed 3D overdensities in SDSS. Although this sample is larger than ours (217 clusters compared to 180) it still seems that there are few systems below $<10^{14}M_{\odot}$ (see their Figure 9). Most confirmed Abell overdensities are rich systems, which explain the figure (note that the open symbols are the X-ray systems, which contain the lower mass objects). The main conclusions drawn from these comparisons are: (i) the slopes of the scaling relations become flatter for high-mass samples, but the differences are within $1-\sigma$; (ii) although the samples of POP05 and Popesso et al. (2007) show fewer systems with low mass, their results are consistent with ours. That is due to the inclusion of a few groups in their sample and to the small variation in the slope with mass. These results indicate that sample incompleteness has little effect on the scaling relations.

For the relations involving L_X we find the same trend as above, with the high mass systems showing flatter relations. However, some clusters were not considered in the fits due to having only upper limits in the X-ray luminosity estimates. This eliminates points that generally have $L_X < 10^{43}$ ergs/s in Figure 5 (lower right panel). These points would be located above the derived fit and would thus make the relations a little flatter. Our results with all clusters could be biased due to missing some low mass systems with $L_X \sim 10^{43}$ ergs/s, making the relations steeper than it would really be. However, considering the conclusions reached above, we might expect that incompleteness (especially in the low mass regime) has a minor impact in the relations. We also note that the results within R_{500} generally are the ones with smallest scatter when considering L_X .

A result that deserves some comments is the third test shown in Table 2 (rows 5 and 6) where we consider all clusters at $z \leq 0.25$, considering that at $z > 0.10$ the spectroscopic survey of SDSS is no longer complete. The main effect exhibited is the flattening of the scaling relations. That happens because N_{gals} and L_{opt} are still well determined (as they rely on the photometric data), but σ_P and mass are not (see discussion in paper I). If the percentage of clusters without enough spectra is large, the impact in the scaling relations may be important. So, the safest approach is to consider only objects that have complete spectroscopic sampling (as done here and by RD06).

Another important issue concerns the interloper removal procedure (see Wojtak et al. 2007). As discussed in §4 of Lopes et al. (2009) we performed several tests to optimize the “shifting-gapper” technique. The final code seems to work well for systems of all masses, as can be seen from the phase-space diagrams (Lopes et al. 2009). POP05 considers the method of Katgert et al. (2004) (see also den Hartog & Katgert 1996), which also combines the position and velocity information, but makes assumptions

regarding the dynamical state of the cluster. RD06 use the caustic technique to determine the mass profile of the clusters, which involves removal of interlopers in underdense regions of the phase-space diagram. Wojtak et al. (2007) applied several different techniques for interloper removal to real and simulated data. They conclude that some methods have poor performance compared to others, but none of the methods cited above are among the poor performers. Whatever the approach, it must be sufficiently restrictive but not overly lax, otherwise many cluster members will be discarded or few interlopers will be rejected, leading to biased values of σ_p and mass. While there is no particular reason to chose one method over another, the procedure should work for a wide variety of systems (as shown for the method adopted here). We based our choice on the simplicity of the method and on the avoidance of assumptions regarding the dynamics of the cluster (Fadda et al. 1996).

Results from a test with a less rigorous criterion (eliminating fewer interlopers) are shown in rows 3 and 4 of Table 2. The comparison of Tables 1 and 2 reveals no systematic effect on the intercept and slope of the scaling relations when relaxing the interloper removal procedure. The scatter of the relations increases slightly, but the results are still consistent with our original relations and to those in the literature. So, we conclude that our method is robust, rendering similar lists of cluster members than other methods. This is reflected in the good agreement with the velocity dispersions of RD06 and the comparison to the scaling relations of other authors (Kochanek et al. 2003; Lin, Mohr & Stanford 2004; Popesso et al. 2005).

The Halo Occupation Distribution (HOD) relates the number of galaxies within the virial radius and the associated mass, expressed as $N_{gal,R200} \propto M_{200}^{\alpha}$. Hierarchical models of structure formation predict that the number of subhalos within a system is directly proportional to the mass of the parent halo. In other words, $\alpha = 1$. However, different mechanisms (such as a decreasing efficiency of star formation, or an increased merger rate) would imply a decreasing number of galaxies per given mass in higher mass halos, agreeing with $\alpha < 1$ (see discussion in Popesso et al. 2007). Here, we do not intend to investigate the HOD. Our main goals are to provide calibrators to the cluster mass and compare those to determine which one traces mass more accurately. However, it is worth mentioning that the connection between mass and richness we found is indeed consistent with $\alpha < 1$, as most recent results in the literature. In a future work we plan to study in detail the HOD and the factors that could make $\alpha < 1$.

Finally, we would like to comment that when comparing the performance of N_{gals} , L_{opt} and L_X as mass tracers, we find that the optical parameters show relations slightly tighter than L_X . The scatter of M_{500} at fixed N_{gal}^{R500} , L_{opt}^{R500} and L_X^{R500} is (0.43 ± 0.03) , (0.44 ± 0.04) and (0.47 ± 0.05) , respectively. The scatter of M_{200} at fixed N_{gal}^{R200} , L_{opt}^{R200} and L_X^{R200} is (0.46 ± 0.04) , (0.49 ± 0.04) and (0.56 ± 0.06) , respectively. In all cases, the scatter and the slope of the relations are reduced for high mass systems. POP05 argued that the poorer performance of L_X is likely due to the variation in the compactness of the galaxy clusters. They also investigated if the scatter in the $M-L_X$ relation could be due to cooling core effects, but they find that this accounts for at

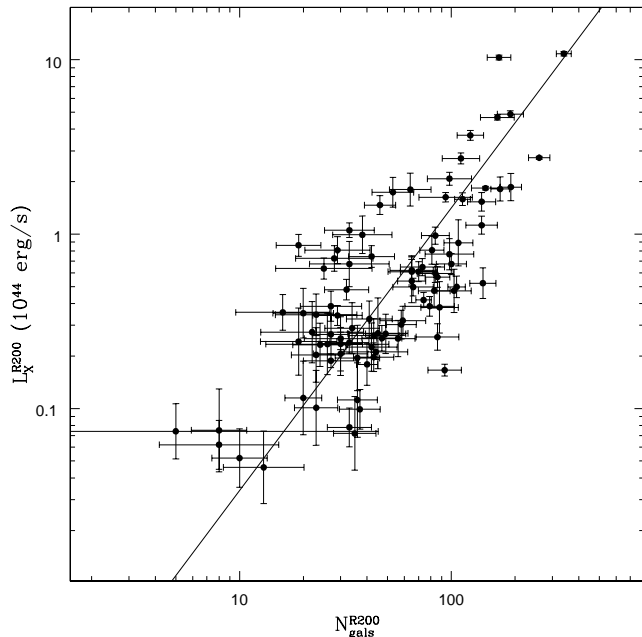


Figure 19. Correlation between X-ray luminosity and richness, both measured within R200. L_X is estimated with the “frame” background.

most 3% of the scatter. The low signal to noise in RASS (especially for the low-mass systems) can also contribute to the higher scatter found in the relations involving L_X . However, it is important to note that here we quote the errors in the scatter, finding that they are all consistent (in the worst case within $1.5\text{-}\sigma$) for the three mass proxies considered (N_{gals} , L_{opt} and L_X).

5 CORRELATION BETWEEN OPTICAL AND X-RAY PROPERTIES

The interplay between global properties obtained in the optical and X-ray regimes are crucial for understanding the complex physics present in galaxy clusters. In recent years a number of works have been dedicated to the comparison of X-ray and optical catalogs or the construction of combined samples (Donahue et al. 2001, 2002; Gilbank et al. 2004; Popesso et al. 2004, 2005; Lopes et al. 2006). The ability to predict the X-ray luminosity or temperature from optical parameters, and vice-versa, is also important for future surveys, conducted only in one regime. As a by-product these comparisons may also reveal unusual clusters (such as X-ray underluminous ones), which are very interesting for follow-up studies.

In this section, we investigate the correlations between optical (N_{gals} and L_{opt}) and X-ray (L_X and T_X) quantities. Note that the X-ray luminosity is estimated through an iterative procedure that assumes the L_X - T_X relation of Markevitch (1998) (see paper I for more details). That relation is close to the self-similar expectations (without any correction for cooling flows in L_X or T_X). This is the same relation adopted to estimate L_X for NORAS, in which $T_X \propto$

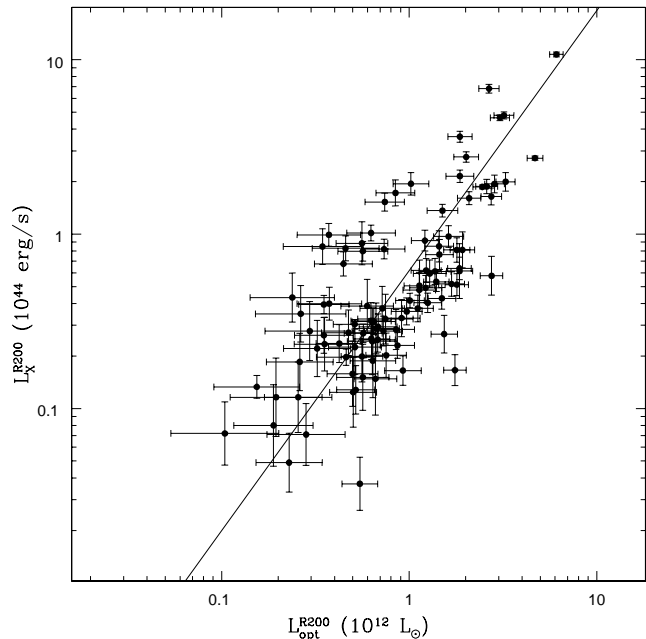


Figure 20. Correlation between X-ray and optical luminosities, both measured within R200. L_X is estimated with the “annulus” background.

$L_X^{1/2}$. Figures 19 and 20 show the connection of L_X to N_{gals} and L_{opt} , respectively. In the first relation L_X is the value obtained with the “frame” background, while the “annulus” background is used in the latter. In both plots, all measurements are performed within R200. Figure 21 shows the correlation between T_X (given by BAX) and L_{opt}^{R200} for 21 clusters.

Table 9 summarizes the fitting parameters for the relations between X-ray and optical measurements within $0.50 \text{ h}^{-1} \text{ Mpc}$, R200, and R500. Note that if one does not have a measure of a radius that scales with mass (R500 or R200), $0.50 \text{ h}^{-1} \text{ Mpc}$ represents the optimal fixed aperture for comparing optical and X-ray properties. Popesso et al. (2004) and Lopes et al. (2006) tested several different fixed apertures and found the scatter to be the smallest when using $0.50 \text{ h}^{-1} \text{ Mpc}$. The results in Table 9 are listed for the two X-ray background types considered (“annulus” and “frame”). In Table 10, we list the results involving T_X (21 clusters found in BAX) for all three apertures used for computing N_{gals} and L_{opt} .

Our results are in good agreement with others in the literature. For instance, POP05, also using data in the SDSS r -band, found similar results to ours: $L_{X,R200} \propto L_{opt,R200}^{1.72}$ and $T_X \propto L_{opt,R200}^{0.61}$. The results within R500 and with a fixed metric (in this case for the i -band) are also close to ours. In the worst cases consistency is found within $1.5\text{-}\sigma$. Donahue et al. (2001) found similar relations but using a different richness definition, which hampers a direct comparison to our findings.

We also find a good agreement to the T_X - N_{gals} and T_X - L_{opt} relations of Lopes et al. (2006). The differences are within $1\text{-}\sigma$. The relations involving L_X are not as similar. Note that in Lopes et al. (2006) we also force a richness cut,

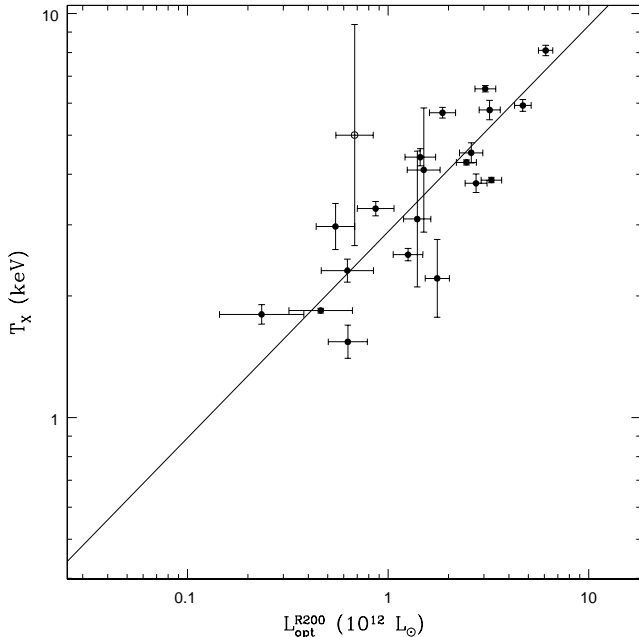


Figure 21. Correlation between temperature and optical luminosity (measured within R200).

with $N_{gals} \geq 10$ (richness within $0.5 h^{-1}$ Mpc). Lopes et al. (2006) also considered optical estimates from DPOSS and X-ray values from BAX. The heterogeneous nature of the luminosities derived from BAX could contribute to the discrepancies. However, the relations involving L_X are much steeper and thus more sensitive to the sample used. If we only consider the most rich clusters the agreement is much better than with the full sample. We also notice that the correlations found in the present work are in excellent agreement with Gal et al. (2009), who used DPOSS data for measuring N_{gals} and L_{opt} within $0.50 h^{-1}$ Mpc and directly estimated L_X from RASS, as done here.

If the density profiles for dark matter and intra-cluster gas are self-similar, the following relations hold: $M \propto T^{3/2}$, $T \propto L_X^{1/2}$ and $M \propto L_X^{3/4}$. Assuming mass traces light (constant M/L_{opt}) we would expect that $L_{opt} \propto L_X^{3/4}$ and $L_{opt} \propto T^{3/2}$. If there is also a strict proportionality between L_{opt} and richness, the same relations above are valid for N_{gals} . Our results are consistent within $2\text{-}\sigma$ with these relations. However, if we assume that $T \propto L_X^{2/5}$ (the typically observed result, David et al. 1993) we would have $L_{opt} \propto L_X^{3/5}$, consistent with our findings at $1\text{-}\sigma$.

6 CONNECTION BETWEEN RICHNESS AND RADIUS

We know that the radius and mass of a cluster scale as $R_{200} \propto M_{200}^{1/3}$ and the number of galaxies within R is linked to mass as $N_{gals,R200} \propto M_{200}^\alpha$. If N_{gals} is measured within a fixed aperture then $N_{gals} \propto N_{gals,R200}^\beta$, with $\beta \sim 0.50 - 0.65$ (see discussion in Hansen et al. 2005). Hierarchical models of structure formation predict that the number of sub-halos within a system is directly proportional to the mass of the

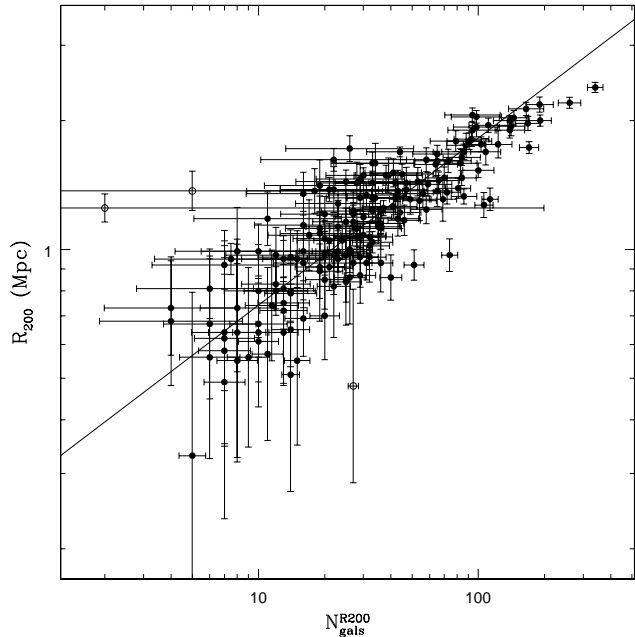


Figure 22. Correlation between radius (R_{200}) and N_{gals}^{R200} .

parent halo, namely $\alpha = 1$. However, different mechanisms such as a decreasing efficiency of star formation, or an increased merger, and destruction rate of galaxies, would imply a decreasing number of galaxies for higher mass halos, suggesting $\alpha < 1$ (see discussion in Popesso et al. 2007). Figure 22 shows the connection between R_{200} and N_{gals}^{R200} , while Table 11 has the solutions for the fits regarding the R_{200} - $N_{gals}^{0.5Mpc/h}$, R_{200} - N_{gals}^{R200} , R_{500} - $N_{gals}^{0.5Mpc/h}$ and R_{500} - N_{gals}^{R500} .

We find $R_{200} \propto N_{gals,R200}^{0.39}$, which indicates that $\alpha = 0.86$. The connection between N_{gals}^{R200} and M_{200} shown in Table 1 indicates $\alpha = 0.93$, agreeing within $1\text{-}\sigma$ to the finding above. The connection between R_{200} and N_{gals} we found is also very close to the result obtained by Gal et al. (2009) who estimated R_{200} photometrically (similar to Hansen et al. 2005), but counted galaxies as in the current work. This agreement corroborates the findings and reliability of the photometric R_{200} estimates given in Gal et al. (2009).

In Table 11 we also list the results relative to optical luminosity. We see that the relations for L_{opt} are consistent to the ones based on richness. These results are also useful for comparison to the slopes of the relations from Popesso et al. (2005). In the SDSS r -band they found that $R_{500} \propto L_{opt,R500}^{0.40}$ and $R_{200} \propto L_{opt,R200}^{0.41}$, in good agreement with our findings.

7 CONCLUSIONS

We have used a sample of 127 NoSOCS plus 56 CIRS galaxy clusters to investigate scaling relations at low redshift ($z \leq 0.10$). For every cluster we previously determined (in paper I) the velocity dispersion (σ_P), physical radii (R_{500} and R_{200}), masses (M_{500} and M_{200}), richness (N_{gals}), optical and X-ray luminosities (L_{opt} and L_X). The last three parameters are estimated within $0.5 h^{-1}$ Mpc, R_{500} and

R_{200} . Substructure estimates are also available for nearly all clusters. We estimated the presence of substructure from the galaxy distribution in two and three dimensions, using the β and Δ tests, respectively. For the CIRS systems we also consider the values of σ_P and M_{200} , independently determined with the caustic method (RD06). For a subset of 21 clusters we have T_X values from the literature and estimated their masses using a M_{200} - T_X relation. The main conclusions we reach are:

(i) Richness, optical and X-ray luminosities correlate well with σ_P and mass. However, the results indicate that the slope and scatter of the relations are higher when using a fixed aperture to compute N_{gals} and L_{opt} . So, the most accurate relations are achieved when considering a physical radius, such as R_{500} and R_{200} . In general, the most accurate results are obtained within R_{500} .

(ii) The scaling relations derived only with the CIRS sample are flatter than the global relations. This indicates that the most massive systems scale differently than the poorer ones. However, the results for the poor and rich systems are still consistent within $1\text{-}\sigma$.

(iii) The scaling relations show no significant modification when considering only clusters without substructure. The new relations, as well as the scatter, are consistent with the original ones. This result holds if we employ a two-dimensional (β) or a three-dimensional (Δ) test. In particular, the 2D test leads to the same scaling relations when we use the spectroscopically or photometric selected galaxy samples.

(iv) The comparison of the scaling relations obtained with optical (virial) and X-ray masses (from the M_{200} - T_X relation) point to very similar results. In other words, the mass calibration with mass estimates from different wavelengths are equivalent. This is one of the main results of this work.

(v) As the velocity dispersions and masses computed with the caustic technique are available in RD06 we have also derived the scaling relations with these parameters (considering the values of N_{gals} , L_{opt} and L_X computed here). Our findings are in line with the conclusions of paper I. Although the slope of the relations agree within $1\text{-}\sigma$ that is only true because the fits obtained with the caustic parameters have a very large scatter. For the M_{200} - L_{opt}^{R200} relation the scatter in mass at fixed luminosity is (0.74 ± 0.18) when using the CIRS results, and only (0.36 ± 0.06) for the virial masses obtained in the current work. The situation is not as critical for the relations based on σ_P , indicating that the interloper removal procedure is not the answer for the observed discrepancies. Instead, these are due to the procedure used for the mass estimation, derived from the caustic mass profile. Uncertainties in this profile lead to different values of R_{200} and as consequence, biased results for M_{200} (see discussion in paper I).

(vi) We find a good agreement with most of the results in the literature, even those derived from other bands (such as 2MASS K). So, the comparison between optical and X-ray properties, the connection between R_{200} and N_{gals} , and the mass calibration performed with different cluster properties, all agree well with previous findings. This also indicates the interloper removal procedure we employed (Lopes et al. 2009) is robust, as other authors we compared to employ

different techniques for selecting cluster members, or even determine mass from other wavelengths.

(vii) The scaling relations based on clusters at $z < 0.25$ are flatter than our original results (considering only objects at $z < 0.10$). However, the results of POP05 – who use clusters in SDSS at $z < 0.25$ – are consistent with our findings. We argue that the fraction of higher- z systems in their sample is probably small, contributing little to their results. However, we acknowledge the relevance of this issue and conclude that clusters' velocity dispersion and masses must be estimated from complete spectroscopic samples (reaching at least $M^* + 1$; see paper I). Using a large sample of clusters having spectra for only the bright members can severely bias σ_P and mass, thus affecting the scaling relations.

(viii) The main result of this paper regards the mass calibration of galaxy clusters. We show that richness, L_{opt} and L_X can reliably be used for mass estimation in the nearby universe. Particularly, the optical properties provide slightly more accurate relations in the present work, which is probably due to the use of RASS in the X-ray regime (shallower than the optical data from SDSS). When considering all clusters, the scatter of M_{500} at fixed N_{gal}^{R500} , L_{opt}^{R500} and L_X^{R500} is (0.43 ± 0.03) , (0.44 ± 0.04) and (0.47 ± 0.05) , respectively. The scatter of M_{200} at fixed N_{gal}^{R200} , L_{opt}^{R200} and L_X^{R200} is (0.46 ± 0.04) , (0.49 ± 0.04) and (0.56 ± 0.06) , respectively. For the richer (CIRS) systems we found the scatter of M_{500} at fixed N_{gal}^{R500} , L_{opt}^{R500} and L_X^{R500} is (0.33 ± 0.05) , (0.38 ± 0.05) and (0.48 ± 0.06) , respectively. These findings are in accord with those of POP05, who found that L_{opt} is a slightly better mass tracer than L_X (also considering SDSS and RASS). This is a very important conclusion, because it tells us that with accurate single band photometry we can reliably estimate the mass of galaxy clusters, a key result for studying the cluster mass function at low redshift. Our work also indicates that the spectroscopic follow-up of a few dozens of clusters to high redshifts ($z \sim 1$) can be used for the understanding of the evolution of the scaling relations and to trace mass at high- z . This is a crucial step for self-calibration methods aiming to constrain the dark energy from the evolution of the cluster population with cosmic time.

Note that we do not state that N_{gals} or L_{opt} are better mass tracers than L_X . We only say that based on RASS and SDSS that is the case. That is due to the fact that RASS is shallow compared to SDSS. A new X-ray survey, for instance based in eROSITA, would provide accurate X-ray luminosities for large samples of clusters. However, as we showed here, richness and optical luminosity are observationally cheap parameters that can also work as a mass proxy. This is an important result for future large sky surveys such as DES, Pan-STARRS, LSST and UKIDSS. If the mass-calibration relation and its evolution are known, these surveys can provide accurate estimates of richness or L_{opt} and thus the mass of clusters at high redshifts.

ACKNOWLEDGMENTS

PAAL was supported by the Fundação de Amparo à Pesquisa do Estado de São Paulo (FAPESP, processes 03/04110-3, 06/57027-4, 06/04955-1 and 07/04655-0). Part of this work was done at the Instituto Nacional de

Astrofísica, Óptica y Electrónica and at the Harvard-Smithsonian Center for Astrophysics. PAAL thanks the hospitality during the stays in these two institutions. C. Jones thanks the Smithsonian Astrophysical Observatory for support. The authors are thankful to A. Biviano for helpful discussions regarding mass estimates of galaxy clusters. We are thankful to Jason Pinkney for making the substructure codes available. We are also thankful for the valuable suggestions made by the referee of this paper.

This research has made use of the NASA/IPAC Extragalactic Database (NED) which is operated by the Jet Propulsion Laboratory, California Institute of Technology, under contract with the National Aeronautics and Space Administration.

Funding for the SDSS and SDSS-II has been provided by the Alfred P. Sloan Foundation, the Participating Institutions, the National Science Foundation, the U.S. Department of Energy, the National Aeronautics and Space Administration, the Japanese Monbukagakusho, the Max Planck Society, and the Higher Education Funding Council for England. The SDSS Web Site is <http://www.sdss.org/>.

The SDSS is managed by the Astrophysical Research Consortium for the Participating Institutions. The Participating Institutions are the American Museum of Natural History, Astrophysical Institute Potsdam, University of Basel, University of Cambridge, Case Western Reserve University, University of Chicago, Drexel University, Fermilab, the Institute for Advanced Study, the Japan Participation Group, Johns Hopkins University, the Joint Institute for Nuclear Astrophysics, the Kavli Institute for Particle Astrophysics and Cosmology, the Korean Scientist Group, the Chinese Academy of Sciences (LAMOST), Los Alamos National Laboratory, the Max-Planck-Institute for Astronomy (MPIA), the Max-Planck-Institute for Astrophysics (MPA), New Mexico State University, Ohio State University, University of Pittsburgh, University of Portsmouth, Princeton University, the United States Naval Observatory, and the University of Washington.

REFERENCES

- Akritas M., & Bershadly M., 1996, *ApJ*, 470, 706
 Becker M.R., McKay T.A., Koester B., Wechsler R.H., Rozo E., Evrard A., Johnston D., Sheldon E., Annis J., Lau E. 2007, *ApJ*, 669, 905
 Bahcall N. A., Comerford J.M. 2002, *ApJ*, 565, L5
 Biviano A., Murante G., Borgani S., Diaferio A., Dolag K., Girardi M. 2006, *A&A*, 456, 23
 Carroll S.M., Press W.H., Turner E.L. 1992, *ARA&A* 30, 499
 David L.P., Slyz A., Jones C., Forman W., Vrtilke S.D., Arnaud K.A. 1993, *ApJ*, 412, 479
 den Hartog R., & Katgert P. 1996, *MNRAS*, 279, 349
 Djorgovski S.G., de Carvalho R.R., Gal R.R., Odewahn S.C., Mahabal A.A., Brunner R.J., Lopes P.A.A., Kohl Moreira J.L. 2003, *Bulletin of the Astronomical Society of Brazil*, 23, 197
 Donahue M., Mack J., Scharf C. et al. 2001, *ApJ*, 552, L93
 Donahue M., Scharf C., Mack J., et al. 2002, *ApJ*, 569, 689
 Dressler A., & Shectman S.A. 1988, *AJ*, 95, 985 (DS)
 Eke V., Cole S., Frenk C.S. 1996, *MNRAS* 282, 263
 Ettori S., Tozzi P., Borgani S., Rosati P. 2004, *A&A*, 417, 13
 Fadda D., Girardi M., Giuricin G., et al. 1996, *ApJ*, 473, 670
 Frieman J.A., Turner M.S., Huterer D. 2008, *ARA&A*, 46, 385
 Gal R.R., de Carvalho R.R., Odewahn S.C., Djorgovski S.G., Mahabal A.A., Brunner R.J., Lopes P.A.A. 2004, *AJ*, 128, 3082
 Gal R.R., de Carvalho R.R., Lopes P.A.A., Djorgovski S.G., Brunner R.J., Mahabal A.A., Odewahn S.C. 2003, *AJ*, 125, 2064
 Gal R.R., Lopes P.A.A., de Carvalho R.R., Kohl-Moreira J.L., Capelato H.V., Djorgovski S.G. 2009, *AJ*, 137, 2981
 Gilbank D. G., Bower R., Castander F., Ziegler B. L. 2004, *MNRAS*, 348, 551
 Girardi M., Giuricin G., Mardirossian F., Mezzetti M., & Boschin W. 1998, *ApJ*, 505, 74
 Hansen S.M., McKay T.A., Wechsler R.H. et al. 2005, *ApJ*, 633, 122
 Henry J.P. & Arnaud K.A. 1991, *ApJ*, 372, 410
 Henry J.P. 2004, *ApJ* 609, 603
 Huterer D., Turner M.S. 2001, *PhRvD*, 64, 13527
 Katgert P., Biviano A., & Mazure A., 2004, *ApJ*, 600, 657
 Kochanek C.S., White M., Huchra J., Macri L., Jarrett T.H., Schneider S.E., Mader J. 2003, *ApJ*, 585, 161
 Levine E.S., Schulz A.E., White M. 2002, *ApJ*, 577, 569
 Lima M. & Hu W. 2004, *PhRvD*, 70, 3504
 Lima M. & Hu W. 2005, *PhRvD*, 72, 3006
 Lin Y., Mohr J., Stanford S. 2004, *ApJ*, 610, 745
 Lopes P.A.A. 2003, Ph.D. Thesis, Observatório Nacional (Brazil)
 Lopes P.A.A., de Carvalho R.R., Gal R.R., Djorgovski S.G., Odewahn S.C., Mahabal A.A., Brunner R.J. 2004, *AJ*, 128, 1017
 Lopes P.A.A., de Carvalho R.R., Capelato H.V., Gal R.R., Djorgovski S.G., Brunner R.J., Odewahn S.C., Mahabal A.A. 2006, *ApJ*, 648, 209
 Lopes P.A.A. 2007, *MNRAS*, 380, 1680
 Lopes P.A.A., de Carvalho R.R., Kohl-Moreira J.L., Jones C. 2009, *MNRAS*, 392, 135, paper I
 Majumdar S., & Mohr J.J. 2004, *ApJ*, 613, 41
 Markevitch M. 1998, *ApJ*, 504, 27
 Navarro J.F., Frenk C.S., White S.D.M. 1997, *ApJ*, 490, 493 (NFW)
 Odewahn S.C., de Carvalho R.R., Gal R.R., Djorgovski S.G., Brunner R.J., Mahabal A.A., Lopes P.A.A., Kohl Moreira J.L., Stalder B. 2004, *AJ*, 128, 3092
 Pinkney J., Roettiger K., Burns J., Bird C. 1996, *ApJS*, 104, 1
 Popesso P., Böhringer H., Brinkmann J., Voges W., York D. 2004, *A&A*, 423, 449
 Popesso P., Biviano A., Böhringer H., Romaniello M., Voges W. 2005, *A&A*, 433, 431, POP05
 Popesso P., Biviano A., Böhringer H., Romaniello M., 2007, *A&A*, 464, 451
 Rines K. & Diaferio A. 2006, *ApJ*, 132, 1275, RD06
 Rosati P., Borgani S., Norman C. 2002, *ARA&A* 40, 539
 Rykoff E.S., McKay T.A., Becker M.R., Evrard A., Johnston D.E., Koester B.P., Rozo E., Sheldon E.S., Wechsler R.H. 2008, *ApJ*, 675, 1106
 Stanek R., Evrard A.E., Böhringer H., Schuecker P., Nord

- B. 2006, ApJ, 648, 956
 Vikhlinin A., VanSpeybroeck L., Markevitch M., Forman W.R., Grego L. 2002, ApJ, 578, L107
 Vikhlinin A., Burenin R.A., Ebeling H., Forman W.R., Hornstrup A., Jones C., Kravtsov A.V., Murray S.S., Nagai D., Quintana H., Voevodkin A. 2008, submitted to ApJ, arXiv: 0805.2207
 West M.J., Oemler A., & Dekel A. 1988, ApJ, 327, 1
 Wojtak R., Lokas E.L., Mamon G.A., Gottlöbber S., Prada F., Moles M. 2007, A&A, 466, 437
 York D.G. et al. 2000, AJ, 120, 1579

APPENDIX A: UPDATE VALUES OF X-RAY LUMINOSITIES

We fixed a bug in the code used to estimate X-ray luminosity and its associated error. Hence we update these values in the table A1 below, which replaces Table 5 from paper I. The meaning of all columns is as in paper I. In the first column we give the cluster name; then in the next three columns we list the values of L_X (and its associated error) for the three backgrounds (“annulus”, “frame” and “boxes”, respectively). In the fifth column we show the X-ray temperature measure from BAX (when available), while the interpolated temperature obtained from the L_X - T_X relation is shown in the sixth column. The last column indicates whether we had a significant detection (SD), an upper limit (UL), or if the measurements should be taken with concern (XX). The cluster is marked as XX if it is too close to a border, or if the background error or net count rates could not be determined. The last two columns of the table are obtained with the “annulus” background.

Table 1. Relations between σ_P , M_{500} and M_{200} to N_{gals} , using three different apertures, 0.50 h⁻¹ Mpc, R_{500} and R_{200} . In all tables the linear fit is of the form $\ln(Y) = A + B \times \ln(X/C)$, where X and Y are listed in the first column. Masses are in units of $10^{14} M_\odot$ and velocity dispersion in km s⁻¹. The results are also shown for three different samples, using the 127 NoSOCS clusters, fifty-three CIRS clusters, and the combination of the two samples with 180 clusters (second column). The intercept (A) and slope (B) are shown in the third and fourth columns, respectively. The scatter in the Y parameter at fixed X is in the fifth column. The total number of clusters for the first fit is shown as N_{tot} and the number of clusters after a 3- σ clip is given by N_{use} . The pivot point depends on the sample, being $C = 25$ for the NoSOCS and full samples and $C = 60$ for the CIRS sample.

Relation X	Y	Sample	A	B	$\sigma_{\ln Y X}$	N_{tot}	N_{use}
$N_{gals}^{0.50}$	σ_P	NoSOCS	5.88 ± 0.03	0.68 ± 0.04	0.29 ± 0.02	127	122
N_{gals}^{R500}	σ_P	NoSOCS	5.80 ± 0.03	0.54 ± 0.03	0.23 ± 0.02	127	124
N_{gals}^{R200}	σ_P	NoSOCS	5.70 ± 0.03	0.56 ± 0.03	0.26 ± 0.03	127	125
$N_{gals}^{0.50}$	M_{200}	NoSOCS	0.75 ± 0.09	1.45 ± 0.16	0.69 ± 0.06	127	124
N_{gals}^{R500}	M_{500}	NoSOCS	0.53 ± 0.06	1.01 ± 0.07	0.53 ± 0.05	127	126
N_{gals}^{R200}	M_{200}	NoSOCS	0.36 ± 0.07	1.09 ± 0.09	0.60 ± 0.07	127	126
$N_{gals}^{0.50}$	σ_P	CIRS	6.49 ± 0.03	0.49 ± 0.05	0.17 ± 0.02	53	51
N_{gals}^{R500}	σ_P	CIRS	6.29 ± 0.02	0.40 ± 0.03	0.14 ± 0.02	53	51
N_{gals}^{R200}	σ_P	CIRS	6.20 ± 0.03	0.41 ± 0.03	0.15 ± 0.01	53	51
$N_{gals}^{0.50}$	M_{200}	CIRS	2.15 ± 0.08	1.36 ± 0.19	0.46 ± 0.08	53	52
N_{gals}^{R500}	M_{500}	CIRS	1.54 ± 0.05	0.95 ± 0.09	0.33 ± 0.05	53	52
N_{gals}^{R200}	M_{200}	CIRS	1.39 ± 0.07	1.00 ± 0.11	0.37 ± 0.05	53	52
$N_{gals}^{0.50}$	σ_P	ALL	5.91 ± 0.02	0.69 ± 0.03	0.25 ± 0.02	180	171
N_{gals}^{R500}	σ_P	ALL	5.81 ± 0.02	0.52 ± 0.02	0.19 ± 0.01	180	175
N_{gals}^{R200}	σ_P	ALL	5.69 ± 0.02	0.53 ± 0.02	0.22 ± 0.02	180	178
$N_{gals}^{0.50}$	M_{200}	ALL	0.79 ± 0.05	1.50 ± 0.08	0.57 ± 0.05	180	174
N_{gals}^{R500}	M_{500}	ALL	0.57 ± 0.04	1.04 ± 0.04	0.43 ± 0.03	180	178
N_{gals}^{R200}	M_{200}	ALL	0.37 ± 0.04	1.07 ± 0.04	0.46 ± 0.04	180	177

Table 2. Fit parameters for the σ_P - N_{gals} , M_{200} - N_{gals} relations within R_{200} for three more cases, all based in the NoSOCS sample (same pivot point as in Table 1). Masses are in units of $10^{14} M_\odot$ and velocity dispersion in km s⁻¹. Rows 1 and 2 considers the original (instead of luminosity-weighted) coordinates. Rows 3 and 4 are for the case when we consider a more “relaxed” criteria for rejecting interlopers (described in § 4.1 of paper I), while rows 5 and 6 have the results for all the 219 NoSOCS clusters at $z \leq 0.25$, instead of $z \leq 0.10$. All the columns have the same meaning as in Table 1.

Relation X	Y	Sample	A	B	$\sigma_{\ln Y X}$	N_{tot}	N_{use}
N_{gals}^{R200}	σ_P	NoSOCS	5.72 ± 0.03	0.54 ± 0.04	0.29 ± 0.03	128	127
N_{gals}^{R200}	M_{200}	NoSOCS	0.38 ± 0.06	1.05 ± 0.09	0.60 ± 0.07	128	127
N_{gals}^{R200}	σ_P	NoSOCS	5.77 ± 0.03	0.58 ± 0.04	0.29 ± 0.04	130	128
N_{gals}^{R200}	M_{200}	NoSOCS	0.51 ± 0.07	1.16 ± 0.09	0.66 ± 0.09	130	129
N_{gals}^{R200}	σ_P	NoSOCS	5.63 ± 0.02	0.43 ± 0.02	0.26 ± 0.02	219	216
N_{gals}^{R200}	M_{200}	NoSOCS	0.21 ± 0.04	0.83 ± 0.05	0.61 ± 0.05	219	216

Table 3. Analogous to Table 1, but listing the fit parameters for the relations of σ_P , M_{500} and M_{200} to L_{opt} . Masses are in units of $10^{14} M_\odot$ and velocity dispersion in km s^{-1} . As before, the pivot point depends on the sample, being $C = 0.40 \cdot 10^{12} L_\odot$ for the NoSOCS and full samples and $C = 1.10 \cdot 10^{12} L_\odot$ for the CIRS sample.

Relation X	Y	Sample	A	B	$\sigma_{\ln Y X}$	N_{tot}	N_{use}
$L_{opt}^{0.50}$	σ_P	NoSOCS	5.88 ± 0.05	0.93 ± 0.10	0.41 ± 0.04	127	124
L_{opt}^{R500}	σ_P	NoSOCS	5.79 ± 0.03	0.63 ± 0.04	0.26 ± 0.02	127	123
L_{opt}^{R200}	σ_P	NoSOCS	5.68 ± 0.04	0.64 ± 0.05	0.38 ± 0.05	127	125
$L_{opt}^{0.50}$	M_{200}	NoSOCS	0.76 ± 0.13	2.00 ± 0.32	0.92 ± 0.20	127	124
L_{opt}^{R500}	M_{500}	NoSOCS	0.51 ± 0.06	1.09 ± 0.07	0.57 ± 0.06	127	125
L_{opt}^{R200}	M_{200}	NoSOCS	0.27 ± 0.07	1.18 ± 0.09	0.63 ± 0.08	127	123
$L_{opt}^{0.50}$	σ_P	CIRS	6.55 ± 0.04	0.59 ± 0.07	0.20 ± 0.03	53	52
L_{opt}^{R500}	σ_P	CIRS	6.31 ± 0.02	0.41 ± 0.03	0.14 ± 0.01	53	50
L_{opt}^{R200}	σ_P	CIRS	6.22 ± 0.03	0.39 ± 0.03	0.15 ± 0.02	53	51
$L_{opt}^{0.50}$	M_{200}	CIRS	2.26 ± 0.11	1.48 ± 0.22	0.57 ± 0.10	53	53
L_{opt}^{R500}	M_{500}	CIRS	1.57 ± 0.05	0.99 ± 0.10	0.38 ± 0.05	53	53
L_{opt}^{R200}	M_{200}	CIRS	1.41 ± 0.06	0.98 ± 0.11	0.36 ± 0.06	53	51
$L_{opt}^{0.50}$	σ_P	ALL	5.85 ± 0.03	0.78 ± 0.05	0.31 ± 0.02	180	178
L_{opt}^{R500}	σ_P	ALL	5.76 ± 0.02	0.56 ± 0.02	0.21 ± 0.02	180	174
L_{opt}^{R200}	σ_P	ALL	5.65 ± 0.03	0.55 ± 0.02	0.24 ± 0.02	180	176
$L_{opt}^{0.50}$	M_{200}	ALL	0.68 ± 0.07	1.70 ± 0.12	0.72 ± 0.07	180	178
L_{opt}^{R500}	M_{500}	ALL	0.49 ± 0.04	1.06 ± 0.04	0.44 ± 0.04	180	173
L_{opt}^{R200}	M_{200}	ALL	0.28 ± 0.05	1.11 ± 0.04	0.49 ± 0.04	180	174

Table 4. Fit parameters for the σ_P - L_X , M_{500} - L_X , M_{200} - L_X relations using two different apertures, R_{500} and R_{200} . The results consider the X-ray luminosity obtained with the “annulus” background (second column). Masses are in units of $10^{14} M_\odot$ and velocity dispersion in km s^{-1} . First we show the results derived with all clusters, then only the CIRS systems are used. The remaining columns have the same meaning as in the previous tables. The pivot points are $C = 0.20 \cdot 10^{44} \text{ erg/s}$ for the full sample and $C = 0.55 \cdot 10^{44} \text{ erg/s}$ for the CIRS sample.

Relation X	Y	Bkg Type	Sample	A	B	$\sigma_{\ln Y X}$	N_{tot}	N_{use}
L_X^{R500}	σ_P	Annulus	ALL	5.90 ± 0.03	0.26 ± 0.03	0.29 ± 0.04	104	104
L_X^{R200}	σ_P	Annulus	ALL	5.85 ± 0.04	0.27 ± 0.03	0.29 ± 0.03	97	97
L_X^{R500}	M_{500}	Annulus	ALL	0.68 ± 0.06	0.62 ± 0.04	0.47 ± 0.05	104	103
L_X^{R200}	M_{200}	Annulus	ALL	0.59 ± 0.08	0.67 ± 0.06	0.56 ± 0.06	97	97
L_X^{R500}	σ_P	Annulus	CIRS	6.21 ± 0.04	0.18 ± 0.04	0.26 ± 0.03	52	52
L_X^{R200}	σ_P	Annulus	CIRS	6.19 ± 0.04	0.19 ± 0.04	0.25 ± 0.03	52	52
L_X^{R500}	M_{500}	Annulus	CIRS	1.39 ± 0.08	0.49 ± 0.08	0.48 ± 0.06	52	52
L_X^{R200}	M_{200}	Annulus	CIRS	1.40 ± 0.08	0.52 ± 0.08	0.49 ± 0.06	52	52

Table 5. Analogous to the previous table, but for the results based in the “frame” background. Masses are in units of $10^{14} M_{\odot}$ and velocity dispersion in km s^{-1} .

Relation X	Y	Bkg Type	Sample	A	B	$\sigma_{\ln Y X}$	N_{tot}	N_{use}
L_X^{R500}	σ_P	Frame	ALL	5.92 ± 0.03	0.24 ± 0.02	0.28 ± 0.04	98	98
L_X^{R200}	σ_P	Frame	ALL	5.90 ± 0.04	0.22 ± 0.03	0.28 ± 0.03	90	90
L_X^{R500}	M_{500}	Frame	ALL	0.73 ± 0.06	0.59 ± 0.04	0.46 ± 0.04	98	96
L_X^{R200}	M_{200}	Frame	ALL	0.68 ± 0.08	0.61 ± 0.06	0.55 ± 0.05	90	89
L_X^{R500}	σ_P	Frame	CIRS	6.20 ± 0.04	0.18 ± 0.04	0.26 ± 0.03	50	50
L_X^{R200}	σ_P	Frame	CIRS	6.19 ± 0.04	0.18 ± 0.03	0.25 ± 0.03	49	49
L_X^{R500}	M_{500}	Frame	CIRS	1.38 ± 0.08	0.49 ± 0.07	0.49 ± 0.06	50	50
L_X^{R200}	M_{200}	Frame	CIRS	1.40 ± 0.08	0.50 ± 0.07	0.50 ± 0.06	49	49

Table 6. Fit parameters for the M_{200} - N_{gals} and M_{200} - L_{opt} for clusters with or without substructure. Masses are in units of $10^{14} M_{\odot}$ and velocity dispersion in km s^{-1} . First, we show (lines 1-6) the results considering an aperture of R_{200} for all clusters and for the substructure free systems. These are selected with the Δ or β tests, applied only to galaxies considered as cluster members (§4). Then we show the results considering the same aperture and the 2-D test (β), but using the photometric sample (no restriction to galaxies with spectra). That is seen in rows 7-10. Finally, we list the results with a fixed metric of $1.5 \text{ h}^{-1} \text{ Mpc}$ for estimating substructure and using the β test. Again, the photometric data are considered (rows 11-14). The parameters of each relation are listed in column 1, while the substructure test (when it is the case) is shown in column 2. The remaining columns have the same meaning as in the previous tables. The pivot points for all samples are $C = 25$ when considering richness, and $C = 0.40 \cdot 10^{12} L_{\odot}$ for L_{opt} .

Relation X	Y	Sub-test	Sample	A	B	$\sigma_{\ln Y X}$	N_{tot}	N_{use}
N_{gals}^{R200}	M_{200}		ALL	0.40 ± 0.05	1.10 ± 0.05	0.48 ± 0.04	170	167
N_{gals}^{R200}	M_{200}	Δ	Sub-free	0.40 ± 0.05	1.10 ± 0.06	0.49 ± 0.05	131	129
N_{gals}^{R200}	M_{200}	β	Sub-free	0.40 ± 0.05	1.10 ± 0.05	0.49 ± 0.04	144	141
L_{opt}^{R200}	M_{200}		ALL	0.31 ± 0.05	1.12 ± 0.05	0.51 ± 0.04	170	163
L_{opt}^{R200}	M_{200}	Δ	Sub-free	0.35 ± 0.06	1.08 ± 0.07	0.52 ± 0.06	131	127
L_{opt}^{R200}	M_{200}	β	Sub-free	0.33 ± 0.05	1.12 ± 0.05	0.53 ± 0.04	144	138
N_{gals}^{R200}	M_{200}		ALL	0.38 ± 0.04	1.09 ± 0.04	0.48 ± 0.03	179	176
N_{gals}^{R200}	M_{200}	β	Sub-free	0.38 ± 0.05	1.06 ± 0.05	0.48 ± 0.04	136	133
L_{opt}^{R200}	M_{200}		ALL	0.28 ± 0.05	1.12 ± 0.05	0.52 ± 0.04	179	173
L_{opt}^{R200}	M_{200}	β	Sub-free	0.33 ± 0.06	1.07 ± 0.06	0.51 ± 0.05	136	131
$N_{gals}^{0.50}$	M_{200}		ALL	0.80 ± 0.05	1.54 ± 0.09	0.64 ± 0.06	183	177
$N_{gals}^{0.50}$	M_{200}	β	Sub-free	0.79 ± 0.06	1.66 ± 0.12	0.59 ± 0.07	119	117
$L_{opt}^{0.50}$	M_{200}		ALL	0.69 ± 0.07	1.74 ± 0.13	0.79 ± 0.08	183	181
$L_{opt}^{0.50}$	M_{200}	β	Sub-free	0.70 ± 0.07	1.72 ± 0.13	0.70 ± 0.08	119	116

Table 7. Fit parameters for the relations connecting M_{200} and σ_P with N_{gals} , L_{opt} and L_X . These last parameters are determined within R_{200} . Masses are in units of $10^{14} M_\odot$ and velocity dispersion in km s^{-1} . The parameters of each relation are listed in column 1. In the second column, we indicate the method used for estimating mass or σ_P . Mass can be derived from the M_{200} - T_X relation of POP05 or from the caustic (RD06). Velocity dispersion values come from the latter (RD06). Relations derived with the first method (masses estimated from T_X) are based in the 21 clusters with temperature available. Results obtained with the second method (considering the caustic values) use the 53 CIRS clusters. The pivot points are the same as listed in the previous tables when considering the CIRS sample. For the 21 rich clusters with T_X available the pivot points are assumed the same. The remaining columns have the same meaning as in the tables above.

Relation X	Y	Mass	A	B	$\sigma_{\ln Y X}$	N_{tot}	N_{use}
N_{gals}^{R200}	M_{200}	X-ray	0.90 ± 0.10	0.92 ± 0.10	0.34 ± 0.08	21	20
L_{opt}^{R200}	M_{200}	X-ray	0.99 ± 0.10	0.85 ± 0.11	0.33 ± 0.08	21	20
L_X^{R200a}	M_{200}	X-ray	1.15 ± 0.14	0.39 ± 0.10	0.36 ± 0.11	20	20
L_X^{R200b}	M_{200}	X-ray	1.02 ± 0.12	0.47 ± 0.08	0.25 ± 0.07	19	18
N_{gals}^{R200}	σ_P	Caustic	6.34 ± 0.03	0.27 ± 0.06	0.18 ± 0.02	53	52
L_{opt}^{R200}	σ_P	Caustic	6.36 ± 0.03	0.25 ± 0.05	0.18 ± 0.03	53	52
L_X^{R200a}	σ_P	Caustic	6.36 ± 0.03	0.12 ± 0.03	0.21 ± 0.03	52	51
L_X^{R200b}	σ_P	Caustic	6.35 ± 0.03	0.12 ± 0.03	0.21 ± 0.03	49	48
N_{gals}^{R200}	M_{200}	Caustic	0.64 ± 0.14	1.35 ± 0.34	0.77 ± 0.22	53	53
L_{opt}^{R200}	M_{200}	Caustic	0.72 ± 0.12	1.26 ± 0.29	0.74 ± 0.18	53	53
L_X^{R200a}	M_{200}	Caustic	0.73 ± 0.13	0.56 ± 0.19	0.87 ± 0.12	52	52
L_X^{R200b}	M_{200}	Caustic	0.68 ± 0.12	0.54 ± 0.15	0.87 ± 0.12	49	49

a – L_X^{R200} estimated with the “annulus” background; b – L_X^{R200} estimated with the “frame” background

Table 8. Slope and orthogonal scatter of different scaling relations, from this work or from other authors. Masses are in units of $10^{14} M_{\odot}$ and velocity dispersion in km s^{-1} . The parameters involved in each relation are listed in column 1; the sample considered is in column 2; the source in columns 3; while the slope and scatter are in columns 4 and 5, respectively.

Relation X	Y	Sample	Source	B	$\sigma_{\ln Y X}$
N^{R500}_{gals}	M_{500}	ALL	This work	1.04	0.43
N^{R200}_{gals}	M_{200}	ALL	This work	1.07	0.46
L^{R500}_{opt}	M_{500}	ALL	This work	1.06	0.44
L^{R200}_{opt}	M_{200}	ALL	This work	1.11	0.49
L^{R500}_{opt}	M_{500}	Extended	Pop05	1.09	0.50
L^{R200}_{opt}	M_{200}	Extended	Pop05	1.06	0.51
$L^R_X a$	M_{500}	ALL	This work	0.62	0.47
$L^R_X a$	M_{200}	ALL	This work	0.67	0.56
$L^R_X b$	M_{500}	ALL	This work	0.59	0.46
$L^R_X b$	M_{200}	ALL	This work	0.61	0.55
L_X	M_{500}	Extended	Pop05	0.59	0.59
L_X	M_{200}	Extended	Pop05	0.60	0.54
L_X	M	—	Sta06	0.63	0.43
L_X	M_{500}	—	Vik08	0.62	0.25
L_X	M	—	Ett04	0.53	0.25
L^{R500}_{opt}	σ_P	ALL	This work	0.55	0.24
L^{R200}_{opt}	σ_P	ALL	This work	0.56	0.21
L^{R500}_{opt}	σ_P	Extended	Pop05	0.43	0.17
L^{R200}_{opt}	σ_P	Extended	Pop05	0.43	0.17
$L^R_X a$	σ_P	ALL	This work	0.26	0.29
$L^R_X b$	σ_P	ALL	This work	0.24	0.28
L_X	σ_P	Extended	Pop05	0.27	0.25

a – $L^R_X a$ estimated with the “annulus” background; b – $L^R_X b$ estimated with the “frame” background. The works of Pop05, Sta06, Vik08 and Ett04 are Popesso et al. (2005); Stanek et al. (2006); Vikhlinin et al. (2008) and Ettori et al. (2004), respectively. Note that the results from Stanek et al. (2006) are dependent of the cosmology. When considering results from the third year of WMAP, they find a reduced scatter $\sigma_{\ln M|L_X} = 0.25$, consistent to Vikhlinin et al. (2008).

Table 9. Fit parameters for the relations between X-ray luminosity (L_X) and optical properties (N_{gals} and L_{opt}) within three different apertures. The aperture used for computing L_X is always the same as indicated for N_{gals} or L_{opt} . L_X is measured in units of 10^{44} erg/s. The background type considered for the L_X estimates is listed in the second column. The sample used for deriving the relations is shown in the third column. The remaining columns are as in Table 1. The pivot points are $C = 25$ when considering richness, and $C = 0.40 \cdot 10^{12} L_\odot$ for L_{opt} .

Relation X	Y	Bkg Type	Sample	A	B	$\sigma_{\ln Y X}$	N_{tot}	N_{use}
$N_{gals}^{0.50}$	L_X	Annulus	ALL	-1.51 ± 0.09	2.28 ± 0.20	0.83 ± 0.13	105	105
N_{gals}^{R500}	L_X	Annulus	ALL	-1.69 ± 0.09	1.64 ± 0.10	0.62 ± 0.09	104	103
N_{gals}^{R200}	L_X	Annulus	ALL	-1.85 ± 0.12	1.59 ± 0.12	0.63 ± 0.09	97	97
$L_{opt}^{0.50}$	L_X	Annulus	ALL	-1.68 ± 0.12	2.38 ± 0.23	0.97 ± 0.19	105	104
L_{opt}^{R500}	L_X	Annulus	ALL	-1.77 ± 0.10	1.62 ± 0.11	0.65 ± 0.10	104	103
L_{opt}^{R200}	L_X	Annulus	ALL	-1.84 ± 0.13	1.49 ± 0.12	0.64 ± 0.10	97	97
$N_{gals}^{0.50}$	L_X	Frame	ALL	-1.47 ± 0.09	2.24 ± 0.20	0.82 ± 0.13	103	103
N_{gals}^{R500}	L_X	Frame	ALL	-1.71 ± 0.09	1.69 ± 0.11	0.68 ± 0.10	98	98
N_{gals}^{R200}	L_X	Frame	ALL	-1.88 ± 0.12	1.62 ± 0.12	0.75 ± 0.11	90	90
$L_{opt}^{0.50}$	L_X	Frame	ALL	-1.63 ± 0.12	2.34 ± 0.23	0.96 ± 0.20	103	102
L_{opt}^{R500}	L_X	Frame	ALL	-1.73 ± 0.10	1.61 ± 0.11	0.68 ± 0.11	98	97
L_{opt}^{R200}	L_X	Frame	ALL	-1.99 ± 0.13	1.59 ± 0.13	0.78 ± 0.14	90	89

Table 10. Fit parameters for the relations between X-ray temperature T_X (in keV) and optical properties (N_{gals} and L_{opt}) within three different apertures. Only the 21 clusters with x-ray temperature available in BAX are used in the fits. That is indicated in the second column (“sample”). The remaining columns are as in the previous table. The pivot points are $C = 60$ when considering richness, and $C = 1.10 \cdot 10^{12} L_\odot$ for L_{opt} .

Relation X	Y	Sample	A	B	$\sigma_{\ln Y X}$	N_{tot}	N_{use}
$N_{gals}^{0.50}$	T_X	BAX	1.52 ± 0.05	0.73 ± 0.11	0.20 ± 0.05	21	21
N_{gals}^{R500}	T_X	BAX	1.22 ± 0.06	0.50 ± 0.07	0.19 ± 0.04	21	21
N_{gals}^{R200}	T_X	BAX	1.05 ± 0.06	0.56 ± 0.06	0.21 ± 0.05	21	20
$L_{opt}^{0.50}$	T_X	BAX	1.56 ± 0.07	0.69 ± 0.13	0.23 ± 0.05	21	21
L_{opt}^{R500}	T_X	BAX	1.21 ± 0.06	0.52 ± 0.07	0.20 ± 0.04	21	20
L_{opt}^{R200}	T_X	BAX	1.10 ± 0.06	0.51 ± 0.06	0.21 ± 0.04	21	20

Table 11. Fit parameters for the R_{500} - N_{gals} , R_{200} - N_{gals} , R_{500} - L_{opt} and R_{200} - L_{opt} relations using three different apertures for computing N_{gals} or L_{opt} . The physical radii are measured in Mpc. The remaining columns are as in the previous table. The pivot points are $C = 25$ when considering richness, and $C = 0.40 \cdot 10^{12} L_{\odot}$ for L_{opt} .

Relation X	Y	Sample	A	B	$\sigma_{\ln Y X}$	N_{tot}	N_{use}
$N_{gals}^{0.50}$	R_{500}	ALL	-0.12 ± 0.02	0.47 ± 0.02	0.19 ± 0.01	180	173
N_{gals}^{R500}	R_{500}	ALL	-0.19 ± 0.01	0.37 ± 0.01	0.14 ± 0.01	180	175
$N_{gals}^{0.50}$	R_{200}	ALL	0.20 ± 0.02	0.48 ± 0.02	0.19 ± 0.01	180	173
N_{gals}^{R200}	R_{200}	ALL	0.05 ± 0.02	0.39 ± 0.02	0.17 ± 0.01	180	177
$L_{opt}^{0.50}$	R_{500}	ALL	-0.16 ± 0.02	0.56 ± 0.04	0.24 ± 0.02	180	178
L_{opt}^{R500}	R_{500}	ALL	-0.22 ± 0.01	0.40 ± 0.02	0.17 ± 0.01	180	175
$L_{opt}^{0.50}$	R_{200}	ALL	0.16 ± 0.02	0.56 ± 0.04	0.24 ± 0.02	180	178
L_{opt}^{R200}	R_{200}	ALL	0.01 ± 0.02	0.40 ± 0.02	0.18 ± 0.01	180	176

Table A1. X-ray luminosity and temperature of the 183 NoSOCS plus CIRS clusters.

name	L_X (annulus) (10^{44} erg s $^{-1}$)	L_X (frame) (10^{44} erg s $^{-1}$)	L_X (box) (10^{44} erg s $^{-1}$)	T_X (BAX) (keV)	T_X (interp. RASS) (keV)	NOTE
NSCS J121847+484410	0.049 ± 0.019	0.052 ± 0.020	0.051 ± 0.019	—	0.7	SD
NSCS J011502+002441	0.404 ± 0.052	0.497 ± 0.058	0.497 ± 0.056	$2.53^{+0.09}_{-0.09}$	2.1	SD
NSCS J100242+324218	0.395 ± 0.048	0.342 ± 0.045	0.371 ± 0.046	—	2.1	SD

Note. - A portion of this table is shown here for guidance regarding its form and content. A full version is available in the electronic edition of the MNRAS.